Chinese Journal of Aeronautics, (2023), 36(12): 164–184

Chinese Society of Aeronautics and Astronautics
& Beihang University

Chinese Journal of Aeronautics

cja@buaa.edu.cn
www.sciencedirect.com

Thermochemical non-equilibrium flow characteristics of high Mach number inlet in a wide operation range

Chunliang DAI [a], Bo SUN [a,*], Lianjie YUE [b,c], Shengbing ZHOU [d], Changfei ZHUO [a], Changsheng ZHOU [a], Jianyi YU [e]

[a] *School of Mechanical Engineering, Nanjing University of Science and Technology, Nanjing 210094, China*
[b] *State Key Laboratory of High Temperature Gas Dynamics, Institute of Mechanics, Chinese Academy of Sciences, Beijing 100190, China*
[c] *School of Engineering Science, University of Chinese Academy of Sciences, Beijing 100049, China*
[d] *College of Aerospace Engineering, Chongqing University, Chongqing 400044, China*
[e] *Beijing System Design Institute of Electro-mechanic Engineering, Beijing 102308, China*

Received 5 December 2022; revised 3 January 2023; accepted 13 February 2023
Available online 3 August 2023

KEYWORDS

Non-equilibrium;
Scramjet inlet;
Starting ability;
Thermochemical;
Work performance

Abstract The high-temperature non-equilibrium effect is a novel and significant issue in the flows over a high Mach number (above Mach 8) air-breathing vehicle. Thus, this study attempts to investigate the high-temperature non-equilibrium flows of a curved compression two-dimensional scramjet inlet at Mach 8 to 12 utilizing the two-dimensional non-equilibrium RANS calculations. Notably, the thermochemical non-equilibrium gas model can predict the actual high-temperature flows, and the numerical results of the other four thermochemical gas models are only used for comparative analysis. Firstly, the thermochemical non-equilibrium flow fields and work performance of the inlet at Mach 8 to 12 are analyzed. Then, the influences of high-temperature non-equilibrium effects on the starting characteristics of the inlet are investigated. The results reveal that a large separation bubble caused by the cowl shock/lower wall boundary layer interaction appears upstream of the shoulder, at Mach 8. The separation zone size is smaller, and its location is closer to the downstream area while the thermal process changes from frozen to non-equilibrium and then to equilibrium. With the increase of inflow Mach number, the thermochemical non-equilibrium effects in the whole inlet flow field gradually strengthen, so their influences on the overall work performance of the high Mach number inlet are more obvious. The vibrational relaxation or thermal non-equilibrium effects can yield more visible influences on the inlet performance than the chemical non-equilibrium reactions. The inlet in the thermochemical non-equilibrium flow can restart more easily than that in the thermochemical frozen flow. This work should provide a basis for the design and starting ability prediction of the high Mach number inlet in the wide operation range.

* Corresponding author.
E-mail address: hypersun@126.com (B. SUN).

https://doi.org/10.1016/j.cja.2023.07.033

Nomenclature

ρ	Density (unit: kg/m^3)
T	Static temperature (unit: K)
D	Diffusion coefficient (unit: m^2/s)
t	Time term (unit: s)
Y	Mass fraction
P	Static pressure (unit: Pa)
u	Velocity (unit: m/s)
E	Specific total energy (unit: J)
H_s	Specific total enthalpy of species (unit: J/kg)
N_s	Number of molecular species
$\dot{\omega}_s$	Mass generation source term (unit: kg·m^{-3} · s^{-1})

Subscripts

∞	Free stream
i, j	Direction
k	Reaction order
v	Vibrational
tr	Translational-rotational

Abbreviations

TCFG	ThermoChemical Frozen Gas
TCNEG	Thermochemical Non-Equilibrium Gas
TNCFG	Thermal Non-equilibrium Chemical Frozen Gas
CNEG	Chemical Non-Equilibrium Gas
TPG	Thermally Perfect Gas
HLLC	Harten-Lax-van Leer Contact
TVD	Total Variation Diminishing

1. Introduction

An air-breathing propulsion system has some outstanding advantages such as hypersonic cruise, reusability, and high specific impulse.[1,2] As a typical representative of the air-breathing hypersonic propulsion system, scramjet has become the research focus in the aerospace field since the 1940s.[3] In particular, many important issues related to Mach 4 to 7 scramjet have been solved, such as the design of the inlet and nozzle,[4–6] shock train in an isolator,[7,8] fuel mixing,[9,10] and combustion mechanisms.[11,12] Hence, the key technologies of high Mach number (above Mach 8) scramjet should receive more attention in the future.

In July 2004, National Aeronautics and Space Administration (NASA) carried out a series of free flight tests on X-43A research aircraft, and the scramjet cruised at Mach 9.6 for about 10 s and achieved the thrust-drag balance.[13] A Mach 12 Rectangular-to-Elliptical Shape Transition (REST) scramjet[14] was designed and experimentally tested at the University of Queensland, Australia. Wise[15] and Toniato[16] et al. reported the full flow path test of Mach 12 REST scramjet in the T4 reflected shock tunnel and the X3 expansion tube, and the experimental data showed that the successful combustion and robust pressure rise can occur during the engine operation. Chan et al.[17] gave the comparative study of a scramjet and a shock-induced combustion ramjet (shcramjet) at a flight Mach 11 and an altitude of 34.5 km, and found that the fuel-specific impulse of a scramjet is 1450 s, which outperforms the shcramjet with 1109 s. Yao et al.[18] numerically investigated a strut-aided hypersonic scramjet working at Mach 7 to 10 and altitudes of 28 to 40 km, and found that the scramjet engine has net thrust while the dynamic pressure range is below 37 kPa and above 55 kPa, and the final combustion efficiencies can reach 66% to 82%. Jiang[2] and Zhang[19] et al. performed the wind tunnel tests and numerical simulations of a Mach 9 hydrogen fuel Oblique Detonation Ramjet Engine (ODRE), and their results successfully confirmed the ODRE concept and the initiation, transition, and stationary combustion of the oblique detonation wave for the first time. The basic data obtained from the above studies of the flight, ground, and numerical test can better demonstrate the feasibility of the high Mach number scramjet, but there are few special studies on the high Mach number inlets.

The inlet is an indispensable compression part of the high Mach number scramjet,[20] its internal flow field often includes these flow phenomena such as shock wave, shock-shock interaction, and shock-turbulent boundary layer interaction.[21] With the increase of flight Mach number, the flight environment of scramjet can become more complex. The total temperature will exceed 2500 K while the flight Mach number is more than 8, oxygen molecules begin to dissociate and their vibrational energy can be further excited.[22] Once the flight Mach number continues to increase, the nitrogen molecules begin to dissociate when the total temperature is higher than 4000 K.[22] The velocity in the flow channel of the high Mach number scramjet is relatively fast, and the molecular vibrations and dissociation chemical reactions compete with the flow velocity, respectively. And the competition can result in "high-temperature or thermochemical non-equilibrium effects".[22–24] Thereby, different from the flow mechanisms of the Mach 4 to 7 inlets[4,5,25,26] belonging to the category of hypersonic aerodynamics, the inlet flows above Mach 8 should involve the high-temperature gas dynamics due to the non-equilibrium process of the vibrational relaxations and chemical reactions.

In the 1990s, a few early research[27,28] on high Mach number inlets were carried out in the United States, but no relevant literature has been found since then. Minucci and Nagamatsu[27] performed the experimental research on the variable geometry inlet at Mach 8 to 18 in the shock wind with a total pressure of 5.5 MPa and a total temperature of 4100 K. The results showed that the shock-boundary layer interaction and the flow being local non-equilibrium effects cause the complex flow field near the cowl region. After numerically calculating the inlet flows at Mach 10 to 15, Lai et al.[28] found that the large error between the computation results and the experiment may be attributed to the lack of the high-temperature non-equilibrium effect and three-dimensional effect in the calculation, as well as to the uncertainty of the experiment. Unfortunately, due to the lower level of computational fluid dynamics technology and the high-temperature gas dynamics theory, the thermochemical non-equilibrium effects were hardly considered in the early studies of high Mach number inlets.

As computer technology constantly develops, the ability to simulate thermochemical non-equilibrium flows has been greatly improved. Many numerical studies on the high-temperature non-equilibrium effects mainly focus on the external laminar flow of some simple configurations such as the cylinder,[29] spherical body,[30] double cone,[31] and double wedge.[32,33] Valentini et al.[29] simulated the thermochemical non-equilibrium flow of a cylinder in the high enthalpy nitrogen environment using direct molecular simulation with accurate *ab initio* potential energy surfaces, and they addressed two vital problems related to the latest method of high-fidelity simulations of high-enthalpy flows in local thermochemical non-equilibrium. Hong et al.[30] demonstrated the ability of the stagnation point streamline model to predict the thermochemical non-equilibrium effects in the hypersonic spherical body flow. Hao and Wen[31] investigated the hypersonic thermochemical non-equilibrium flows of a double cone in the oxygen environment. It was indicated that the improved thermochemical model can predict a higher peak value of wall heat flux and a larger separation bubble than the conventional two-temperature model, and the change of density is an important factor determining the separated bubble size. Then, Hao et al.[32] numerically calculated the hypervelocity flow fields of the 30°–55° double wedge in the total enthalpy of 8.0 MJ/kg. The results displayed that the high-temperature non-equilibrium effects can decrease the separation bubble length, wall aerodynamic heating, and the standoff distance of the detached shock formed by the second wedge. Vatansever and Celik[33] gave a numerical analysis of the high-enthalpy double-wedge flow with four aft wedge angles. It was found that with the increase of the aft wedge angle, the shock wave interactions strengthen, the magnitude of wall heat flux significantly enhances, and the chemical reaction rates accelerate.

Compared with the external flow mentioned above,[29–33] less attention is paid to the high-temperature non-equilibrium effects of the high Mach number internal flows which are turbulence and have long duration. In recent years, the high-temperature flows in hypersonic inlets and isolators have also been preliminarily studied. Fiévet and Raman[34] found that the vibrational (thermal) non-equilibrium effect can change the leading-edge position and length of the shock train in a dual-model scramjet isolator. Then, Dai et al.[24,35] researched the high-temperature non-equilibrium flows of a two-dimensional inlet and an inward-turning inlet at Mach 12 by employing the Reynolds averaging method with thermochemical non-equilibrium effects. For the Mach 12 two-dimensional inlet,[24] the thermal non-equilibrium effects are the strongest near the interaction zone between the cowl shock and the boundary layer on the lower wall. The dissociation reactions are the strongest in the high-temperature zone of the boundary layer, but the thermal state is close to equilibrium here. Compared with the thermal equilibrium gas model, the compression ratio for the TCNEG model is higher, and its mass coefficient and total pressure recovery coefficient are lower. For the Mach 12 inward turning inlet,[35] the dissociation reactions mainly occur in the boundary layer and the streamwise vortex, and the thermochemical non-equilibrium effect can change the formation and development of the streamwise vortex. Compared with the CNEG model, the dissociation reactions near the inlet wall for the TCNEG model are stronger. Zuo et al.[36] gave the influences of the real-gas effects and wall temperatures on a hypersonic wavecatcher intake at Mach 12. The flow structures and performance of the Mach 12 wavecatcher intake with different wall temperatures were mainly analyzed. However, detailed analyses of thermal and chemical non-equilibrium effects and the reasons why the real gas effect affects the inlet were not provided.

In the previous study,[24,35] we only focused on the high-temperature non-equilibrium effects of the inlet under the design condition of Mach 12. The work capability in the wide operating range and the good starting characteristic are very crucial to the scramjet inlet. The starting characteristics of supersonic/hypersonic inlets[4,25] have been extensively researched, while those of inlets above Mach 8 have not been noticed yet. Using ground wind tunnel tests to simulate the real flight environment above Mach 8 is costly and difficult, so the thermochemical non-equilibrium flow characteristics of the high Mach number inlet in a wide work range are investigated by the numerical calculations in the present work. First, the influences of thermochemical non-equilibrium effects on the flow field and work performance of the scramjet inlet at Mach 8 to 12 are focused on, and then the starting characteristics of the inlet in thermochemical non-equilibrium flows are investigated.

2. Two-dimensional inlet model details

In the incoming flow of a high Mach number, the compression efficiency of a curved surface is better than that of a plane surface.[20] Hence, a simple quadratic function curve $y = a + bx + cx^2$ is used to forward design the curved compression surface of the two-dimensional inlet in this paper, and here a, b, and c all denote constant coefficients. The more details of the forward design method are the same in Ref. 20. The curved compression two-dimensional inlet with the design condition of Mach 12 is shown in Fig. 1. The length of the curved compression surface is 1.588 m, the initial and total deflection angles of it are 4° and 10°, respectively. The heights of the cowl and exit are 0.233 m and 0.033 m, respectively. The distance between the throat and the leading edge is 1.624 m, and the total length of the inlet is 1.888 m. The total contraction ratio being equal to the height ratio of the cowl and throat is 7.061, and the internal contraction ratio being the same as the ratio of the vertical distance from the cowl to lower wall to throat height is 2.242. The intersection of the curved compression surface and the straight section is named the shoulder. The isolator that can avoid the forward propagation of back pressure inside the combustor is the portion from the throat to exit.

3. Mathematical approach

3.1. Conservation equations

The thermochemical non-equilibrium flows of the high Mach number inlet are predicted by solving the two-dimensional compressible Navier-Stokes equations including the two-temperature model, finite-rate chemical reactions, and a two-equation eddy viscosity turbulence model. For the gas flows in the thermal non-equilibrium state, it is necessary to describe the distributions of different internal energy states using different temperatures. In this study, the translational energy can be quickly equilibrated with the rotational energy, so the translational-rotational temperature T_{tr} can be used to

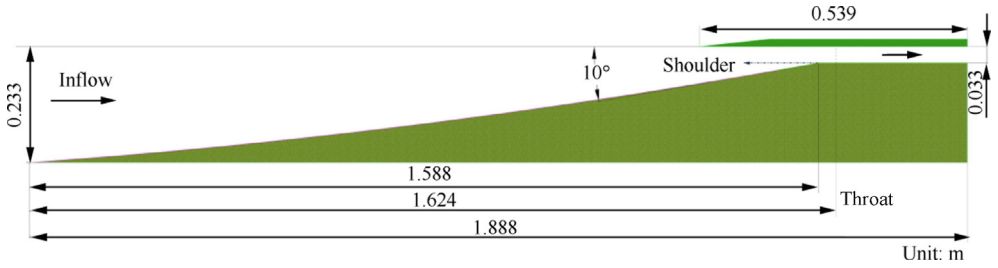

Fig. 1 Configuration of curved compression two-dimensional inlet.

describe the distributions of these two energy states. The maximum temperature in the present study does not exceed 9000 K, so only the vibrational temperature T_v is needed to characterize the vibrational energy state without considering the excitation of electronic energy. The high-temperature air model involves five species (N_2, O_2, NO, N, and O). The conservation equations in Cartesian coordinates are given as follows:

$$\frac{\partial \rho_s}{\partial t}+\frac{\partial \rho_s u_i}{\partial x_i}=\frac{\partial}{\partial x_i}\left(\rho D_s \frac{\partial Y_s}{\partial x_i}\right)+\dot{\omega}_s \tag{1}$$

$$\frac{\partial \rho u_i}{\partial t}+\frac{\partial \rho u_i u_j}{\partial x_j}=-\frac{\partial P}{\partial x_i}+\frac{\partial \tau_{ij}}{\partial x_j} \tag{2}$$

$$\frac{\partial \rho e_v}{\partial t}+\frac{\partial \rho e_v u_i}{\partial x_i}=\frac{\partial}{\partial x_i}\left(q_{v,i}+\sum_{s=1}^{N_s}\rho D_s e_{v,s}\frac{\partial Y_s}{\partial x_i}\right)+\dot{\omega}_v \tag{3}$$

$$\frac{\partial \rho E}{\partial t}+\frac{\partial[(\rho E+P)u_i]}{\partial x_i}=\frac{\partial}{\partial x_i}\left(\tau_{ij}u_i+q_{tr,i}+q_{v,i}+\sum_{s=1}^{N_s}\rho H_s D_s\frac{\partial Y_s}{\partial x_i}\right) \tag{4}$$

where the above four formulations are the conservation equations of mass, momentum, vibrational energy, and total energy, respectively; ρ, u, and P denote the density, velocity, and static pressure, respectively, and the mixture density can be expressed as $\rho=\sum_{s=1}^{N_s}\rho_s$; t represents the time term; x is the axis coordinate; D and Y represent the diffusion coefficient and mass fraction, respectively; $\dot{\omega}_s$ denotes the production mass rate of species s per unit volume; subscripts of s, i, and j are the species, i coordinate direction, and j coordinate direction, respectively; τ_{ij} is each component of the shear stress tensor and expressed as $\tau_{ij}=(\mu_L+\mu_T)\left[\left(\frac{\partial u_i}{\partial x_j}+\frac{\partial u_j}{\partial x_i}\right)-\frac{2}{3}\cdot\frac{\partial u_k}{\partial x_k}\cdot\delta_{ij}\right]$, and μ_L, μ_T, and δ_{ij} are the laminar viscosity, turbulence viscosity, and Kronecker delta, respectively.

In the Eq. (3) and Eq. (4), e_v represents the mixture vibrational energy; $\dot{\omega}_v$ is the source item of the vibrational energy; E denotes the specific total energy and is expressed as $E=e+\frac{1}{2}u_i\cdot u_i$ where e is the mixture internal energy; $q_{tr,i}$, $q_{v,i}$ represent the heat flux in the translational-rotational and vibrational modes, respectively, and they are calculated by adopt Fourier's law ($q_{tr,i}=\lambda_{tr}\cdot(\partial T_{tr}/\partial x_i)$, $q_{v,i}=\lambda_v\cdot(\partial T_v/\partial x_i)$).

3.2. Thermodynamic relationship & chemical reactions

Here, the gas mixture is composed of a variety of single species, and it is assumed that the thermodynamic behavior of every species conforms to the thermally perfect gas. From a partial pressure law of John Dalton, the gas mixture state equation can be written as $P=\rho T\sum_{s=1}^{N_s}R_s Y_s$, where N_s and R_s denote the total number and gas constant of species s, respectively. The ionization of any species need not be considered in this paper, so the total internal energy consists of translational energy, rotational energy, and vibrational energy. The mixture internal energy e and each species internal energy e_s are expressed as $e=\sum_{s=1}^{N_s}e_s$, $e_s=e_t^s+e_r^s+e_v^s+e_{ref}^s$, where e_t^s,e_r^s, and e_v^s denote the species energy in translational, rotational, and vibrational states; e_{ref}^s represents the species formation energy at the reference temperature of 298.16 K.

For molecules, translational and rotational energy can be fully excited, and each species internal energy is calculated as $e_t^s=\frac{3}{2}R_sT, e_r^s=R_sT, e_v^s=R_s\frac{\theta_s}{\exp(\theta_s/T_v)-1}$. Here, θ_s denotes the vibrational characteristic temperature of every molecular species, and θ_s values of O_2, N_2, and NO are 2273 K, 3393 K, and 2739 K, respectively. Yet, the internal energy for each atom species is calculated as $e_t^s=\frac{3}{2}R_sT, e_r^s=0$ J/mol, $e_v^s=0$ J/mol.

The vibrational energy source item $\dot{\omega}_v$ in Eq. (3) can be written as $\dot{\omega}_v=Q_{t\text{-}v}+\sum_{s=1}^{3}\dot{\omega}_s e_v^s$. Here, $Q_{t\text{-}v}$ denotes the translational and vibrational energy relaxation term, and $\sum_{s=1}^{3}\dot{\omega}_s e_v^s$ represents the change amount of vibrational energy caused by the generation term of molecular species. The translational and vibrational energy relaxation process is modeled by employing the Landau-Teller model,[37] so $Q_{t\text{-}v}$ is computed by

$$Q_{t-v}=\sum_{s=1}^{N_s}\rho_s\frac{e_v^s(T)-e_v^s(T_v)}{\tau_s},\ \tau_s=\tau_s^{MW}+\tau_s^{Park} \tag{5}$$

where τ_s^{MW} and τ_s^{Park} represent Millikan-White relaxation time[38] and Park's finite collision time,[39] respectively. These two time items can be written as

$$P\tau_s^{MW}=\frac{\sum_{k=1}^{5}n_k\exp\left[1.16\times10^{-3}\mu_{sk}^{1/2}\theta_s^{4/3}(T^{-1/3}-0.015\mu_{sk}^{1/4})-18.42\right]}{\sum_{k=1}^{5}n_k} \tag{6}$$

$$\tau_s^{Park}=(\sigma_s c_s n_s)^{-1},\ \sigma_s=\left(\frac{50000}{T}\right)^2\times10^{-21},\ c_s=\left(\frac{8KT}{\pi M_s}\right)^{\frac{1}{2}} \tag{7}$$

where the unit of static pressure P is atm (1 atm = 101325 Pa); n_k denotes the number density of species k; μ_{sk} represents the reduced molar mass of species s and k, and it is defined as $\mu_{sk}=(M_s\cdot M_k)/(M_s+M_k)$, M_s represents species molecular weight; σ_s is the effective cross-section area in vibration relaxation processes; c_s denotes the average molar velocity in molecule thermal motions; K represents the Boltzmann constant.

An air species chemical mechanism including five detailed and reversible reaction processes is employed to model chemical non-equilibrium effects in the high Mach number flow, and it is shown in

$$\begin{cases} \text{R1}: \ \mathrm{N_2 + M \leftrightarrow 2N + M} \\ \text{R2}: \ \mathrm{O_2 + M \leftrightarrow 2O + M} \\ \text{R3}: \ \mathrm{NO + M \leftrightarrow N + O + M} \\ \text{R4}: \ \mathrm{NO + O \leftrightarrow O_2 + N} \\ \text{R5}: \ \mathrm{N_2 + O \leftrightarrow NO + N} \end{cases} \tag{8}$$

Reactions R1, R2, and R3 denote the dissociation (forward) and recombination (backward) reaction processes of N_2, O_2, and NO, respectively. Displacement reactions are simulated by employing the last two chemical processes (R4, R5).

In the mass conservation Eq. (1), the source term of species mass productions can be calculated as $\dot{\omega}_s = M_s \sum_{r=1}^{N_r} (\beta_{s,r} - \alpha_{s,r})(R_{f,r} - R_{b,r})$, where N_r denotes the total number of chemical reactions; $\alpha_{s,r}$ and $\beta_{s,r}$ represent the stoichiometric coefficients for reactants and products in the rth reaction, respectively; $R_{f,r}$ and $R_{b,r}$ denote the forward and backward reaction rates of the rth reaction, respectively, and are computed by

$$R_{f,r} = k_{f,r} \prod_{s=1}^{N_s} \left(0.001 \frac{\rho_s}{M_s}\right)^{\alpha_{s,r}}, R_{b,r} = k_{b,r} \prod_{s=1}^{N_s} \left(0.001 \frac{\rho_s}{M_s}\right)^{\beta_{s,r}} \tag{9}$$

Here, $k_{f,r}$ and $k_{b,r}$ represent the forward and backward reaction rate coefficients of the rth reaction, respectively, and they can be calculated through an exponential law formula proposed by Arrhenius, which is written as

$$k_{f,r} = A_k T_c^{B_k} \exp(-E_{ac,r} R_0^{-1} T_c^{-1}), k_{b,r} = k_{f,r}/k_{eq} \tag{10}$$

where A_k, B_k, and $E_{ac,r}$ are the pre-exponential parameter, temperature exponent, and activation energy during the rth reaction process, respectively. The above reaction coefficients are consistent with Ref. 39. To calculate the backward reaction rate coefficient $k_{b,r}$, a chemical reaction equilibrium constant k_{eq} is obtained by applying a Gibbs energy fitting function built by McBride et al.[40].

Generally, the control temperature of reaction rate T_c in thermal equilibrium flows is equal to the translational-rotational temperature (or static temperature). Nevertheless, the coupling influence of the chemical reactions and vibration relaxations in thermochemical non-equilibrium flows should be worthy to be valued. Therefore, a mixing mean temperature T_m is applied for controlling the chemical reaction rate to model the coupling influence, and it can be written as $T_c = T_m = T_{tr}^{\ n} \cdot T_v^{1-n}$; notably, the value of n is 0.5 in dissociation reactions, but should be equal to 1 in other reactions (recombination, displacement).

From different assumptions, the following five thermochemical models are employed in this work, and their main features are presented in Table 1. (A) ThermoChemical Non-Equilibrium Gas (TCNEG): it can be achieved by using the vibrational relaxation and chemistry reaction model presented in Eqs. (5) and (8). (B) Thermal Non-equilibrium and Chemical Frozen Gas (TNCFG): based on the TCNEG model, chemical reactions are assumed not to occur. (C) Thermo Frozen Chemical Frozen Gas (TCFG): both the vibrational relaxation and chemical reaction processes are assumed to be not implemented, and specific heat ratio is equal to 1.4. (D) Chemical Non-Equilibrium Gas (CNEG): vibrational relaxation process is assumed to be in equilibrium, and chemical reaction process is simulated by employing the above chemical mechanism. (E) Thermally Perfect Gas (TPG): based on the CNEG model, chemical reactions are assumed not to occur. Usually, TCFG also called calorically perfect gas is applied to the inviscid design[20] of the inlet, and TPG is utilized to numerically calculate the supersonic flow characteristics[4,5] at Mach 4 to 6, so the TCFG and TPG computing results are regarded as the contrast reference. The TNCFG and CNEG results mainly are used for researching the influence of chemical reactions.

3.3. Computational details & mesh

Laminar transport coefficients (viscosity and thermal conductivity) of each species in the present study are calculated by employing the following fitting functions given by Gupta and Yos[41]. Since the forebody is generally located upstream of the inlet for a high Mach number air-breathing aircraft,[15–17] it is assumed that boundary layer flows inside the inlet have transitioned to turbulence from laminar flow. Considering the calculation efficiency, the Reynolds Averaged Navier-Stokes (RANS) method with the k-ω Shear Stress Transport (SST) model presented by Menter[42] is applied for modeling turbulence flows near the inlet wall. Additionally, the compressible effect correction presented by Sarkar[43] is added to the above turbulence model. The details of the transport coefficients and turbulence model can be seen in Appendix A.[44–47]

The above compressible RANS equation systems are solved by employing the finite volume method. In the time integration, a second-order point implicit scheme[48] with double time-stepping and multi-grid acceleration is utilized for dealing with the coupling source terms of the vibrational relaxation and finite-rate chemical processes, to solve stiffness problems brought by source terms better and accelerate the convergence speed stably. For the spatial discretization, the upwind flux information can be acquired by utilizing a non-linear approximate Riemann solver which is known as Harten-Lax-van Leer Contact (HLLC)[49] and has been widely employed in the supersonic[50] and hypersonic[51] flows. A multi-dimensional TVD (Total Variation Diminishing) approach[52] is employed to avoid introducing new maxima and minima in the reconstruction. A continuous-type limiter is applied for preventing the spurious oscillation phenomenon when solving significant gradients or discontinuities. The above calculation approach that our team developed has been successfully employed to investigate the thermochemical non-equilibrium flows of a double wedge[23] in an environment with stagnation enthalpy of 8.0 MJ/kg, a Mach 12 two-dimensional inlet,[24] and a Mach 12 inward turning inlet.[35]

Fig. 2 displays the computational domain of the two-dimensional curved compression inlet, and it includes 300 thousand structured grids in total. The grids near the mainstream shock wave are locally densified to ensure that hock structures in the inlet flow field can be accurately captured. Furthermore, grids normal to the wall are also partly refined, and the first layer height of them is 1.0×10^{-6} m, guaranteeing that y^+ values on all walls are less than 1. The blue, red, and

Table 1 Main features of five thermochemical gas models.

Item	ThermoChemical Non-Equilibrium Gas (TCNEG)	Thermal Non-equilibrium & Chemical Frozen Gas (TNCFG)	ThermoChemical Frozen Gas (TCFG)	Chemical Non-Equilibrium Gas (CNEG)
Vibrational relaxation	Non-equilibrium	Non-equilibrium	Frozen	Equilibrium
Chemical reaction	Non-equilibrium	Frozen	Frozen	Non-equilibrium

black lines represent the boundaries of the far field, solid wall, and outlet, respectively.

The flight dynamic pressure remains unchanged at 50 kPa in the wide work range, and the free-stream flight parameters at Mach 8 to 12 are presented in Table 2. In the free stream, the vibrational temperature is equal to the static temperature, and mass fractions of oxygen and nitrogen are 0.23 and 0.77 respectively for all Mach number conditions. The far-field boundary is set as the supersonic inflow condition, and all variable parameters such as velocity, static pressure, static temperature, vibrational temperature, and species content are the same as ambient parameters. Since air-breathing vehicles generally work for a long time, we consider that the heat status on inlet surfaces can be in equilibrium with the local airflow, and all solid walls are assumed to be adiabatic and non-slip. Although the inlet solid wall may deform due to the high temperature, this complicated issue cannot be considered in current numerical calculations. The influences of the combustor on its upstream flow field are not considered, so all parameters in the outlet boundary need not be provided, and these can be extrapolated from the interior.

All flow parameters in the far-field boundary are utilized for initializing all numerical calculations, and transient state RANS equation systems presented above are solved by employing the time-marching manner. The convergence criterion in this study is that the steady-state flow field cannot be obtained until the residuals of each equation are less than 1.0×10^{-4}.

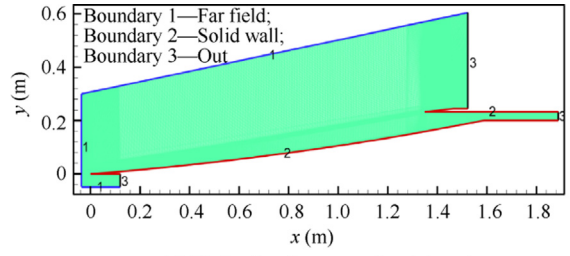

(a) Mesh of total computational domain

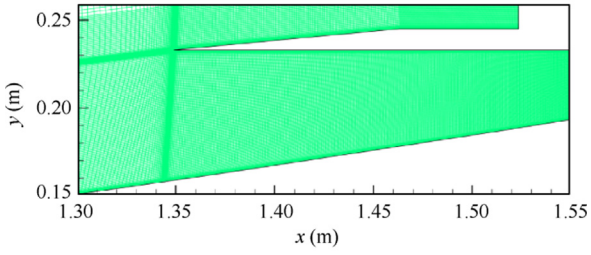

(b) Enlarged view of mesh near cowl

Fig. 2 Computational mesh of two-dimensional curved compression inlet.

3.4. Validation & mesh independence

Firstly, a high-enthalpy double-cone experiment finished by Holden et al.[53] is employed to verify whether the numerical simulation method in this study can effectively predict thermochemical non-equilibrium flows. The wind tunnel inflow conditions are presented as follows: velocity is 4303 m/s, static temperature is 389 K, density is 0.984×10^{-3} kg/m^3, total enthalpy is 9.65 MJ/kg, and unit Reynolds number is 3.9×10^5 m^{-1}. Mass fractions of oxygen and nitrogen are 0.23 and 0.765 respectively. The calculating mesh of the double cone is displayed in Fig. 3, the total number of all structured grids is 50 thousand, and the height of the first layer grids near cone surfaces is 1.0×10^{-6} m. The x-axis is set as axisymmetric condition, all solid walls are regarded as being viscous, non-catalytic, and 300 K isothermal.

Fig. 4 exhibits the Mach number contours and shock structures of the double-cone flow, and there are some typical flow characteristics such as separation bubble, triple point, supersonic jet, and low-speed zone. As revealed in Fig. 5, the static pressure and heat flux on cone surfaces calculated by employing the TCNEG coincide well with the experimental results in Ref. 53. Consequently, we argue that the numerical calculating method presented above should be capable of modeling the thermochemical non-equilibrium flow.

Secondly, the applicability of the TCNEG coupled with the k-ω SST model in the high Mach number turbulence flow is tested by a 34° wedge compression corner experiment[54] at Mach 9.22. Free-stream test conditions are provided as: Mach number is 9.22, unit Reynolds number is 4.7×10^7 m^{-1}, stagnation and static temperature are 1070 K and 64.5 K respectively, and wall temperature is 295 K. The calculating mesh and specific boundary conditions are presented in Fig. 6. Moreover, Fig. 7 reveals the density gradient in the compression corner flow field; the leading-edge shock caused by the boundary layer on the horizontal wall intersects with recompression shock near the ramp, and the flow separation occurs at the corner. Fig. 8 depicts the comparison between wall parameters calculated by the TCNEG coupling k-ω SST model and experiment results. To better compare with the experimental data,[54] P_∞ and Q_∞ are used to make the wall static pressure and heat flux dimensionless. As indicated in Fig. 8(a), the pressure rise distribution of the current computed result at the flow separation starting position is consistent with that of the

Table 2 Free-stream flight parameters at Mach 8 to12.

Ma_∞	U_∞ (m/s)	P_∞ (Pa)	T_∞ (K)	ρ_∞ (kg/m^3)	T_{total} (K)
8	2416.15	1115.92	226.97	1.713×10^{-2}	2685.52
9	2727.52	882.49	228.54	1.345×10^{-2}	3300.75
10	3055.61	714.33	232.33	1.071×10^{-2}	4021.90
11	3387.52	590.41	235.99	8.716×10^{-3}	4825.32
12	3721.84	496.40	239.37	7.225×10^{-3}	5703.55

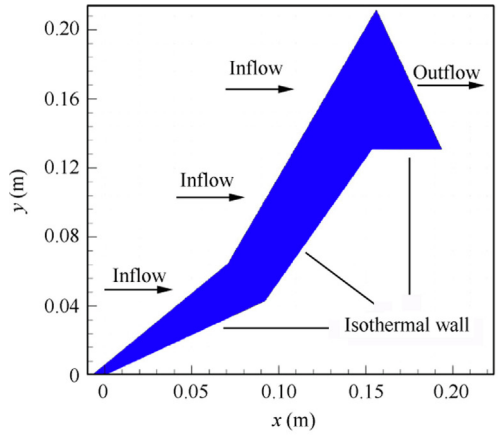

(a) All meshes and boundary conditions

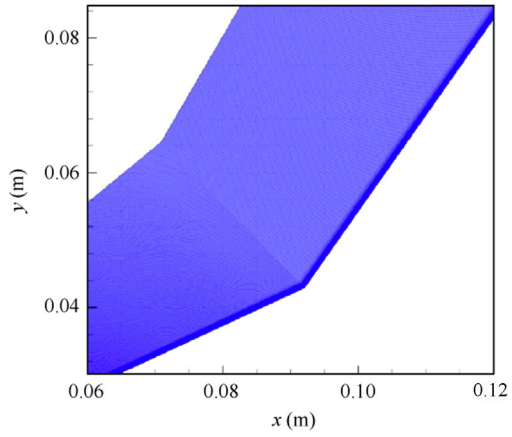

(b) Enlarged view of mesh near compression corner

Fig. 3 Calculating mesh of double cone.

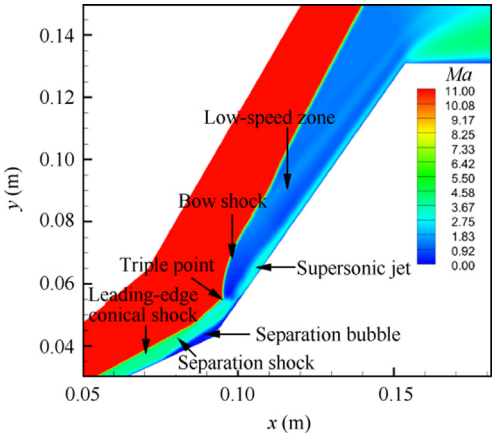

Fig. 4 Mach number contours of double-cone flow.

experiment,[54] but all the published numerical results of Jiang,[55] Tu,[56] and Zhang[57] et al. cannot accurately estimate the separation length. The peak value of static pressure that we give also matches with that of the experiment,[54] yet those of the above published results are 28.6% lower than those of the experiment. Unfortunately, the static pressure peak position of our calculation is downstream of the experimental data, which should be due to the lack of detailed information about the experimental model. The heat flux rate distribution from this calculation through TCNEG coupling k-ω SST model does not show an obvious difference with the experimental trend, which is exhibited in Fig. 8(b). Nevertheless, the above-published results[55–57] may also not show good distributions of the heat flux peak. From the above comparative analyses, the present numerical means can be applied to the prediction of high Mach number turbulence flows.

Furthermore, a mesh-independent investigation of the Mach 12 inlet is carefully completed to check the influence of the number of grids on calculation results. The three kinds of calculation domains are divided employing 2.5×10^5, 3.0×10^5, and 3.5×10^5 structural grid cells, and the heights of their first layer gird on surfaces are all 1.0×10^{-6} m. The TCNEG coupling k-ω SST turbulence model and the inlet configuration presented in Section 2 are utilized in these three numerical calculations. Fig. 9 presents the flow parameters at the exit section calculated with three kinds of calculation mesh, and the parameter distributions of the three kinds of mesh show larger differences in the mainstream zone. From Fig. 9 (a), the maximum deviation value of Mach number between 2.5×10^5 and 3.0×10^5 grids is 3.27%, yet that between 3.0×10^5 and 3.5×10^5 grids is 1.14%. In Fig. 9(b), the maximum deviation value of static temperature between the first two grids is 4.89%, but that between the last two grids is 1.03%. Hence, we argue that the results of 3.0×10^5 grids are convergent and can be applied to the following study work.

4. Results and discussion

4.1. Flow field analysis in starting state

Fig. 10 exhibits the static pressure contours for TCNEG at different inflow Mach numbers. With the increase of inflow Mach number, the leading-edge curved shock angle decreases

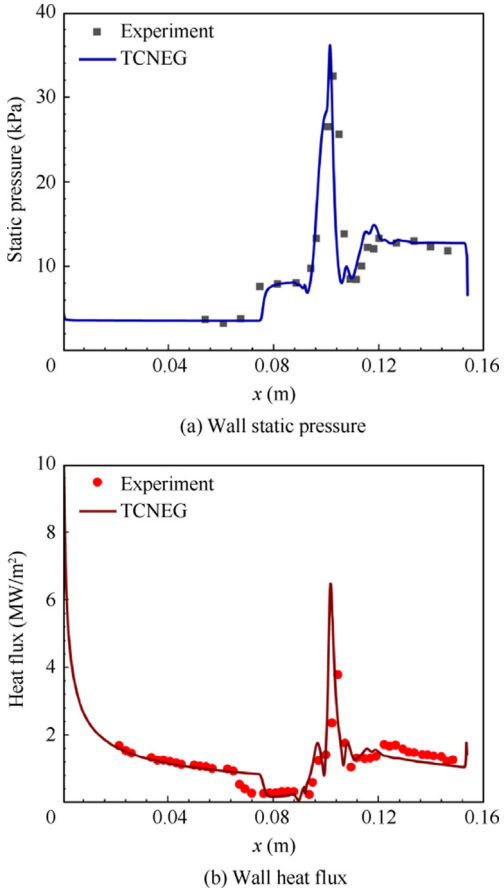

Fig. 5 Comparison between calculating results of TCNEG and experimental data.[53]

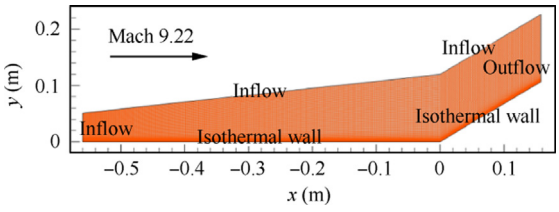

Fig. 6 Calculating mesh of compression corner.

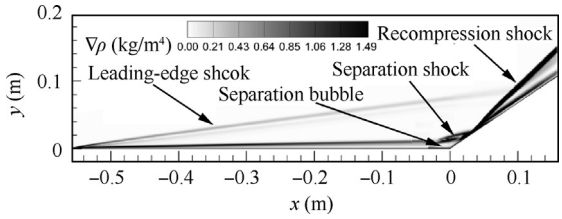

Fig. 7 Density gradient in compression corner flow.

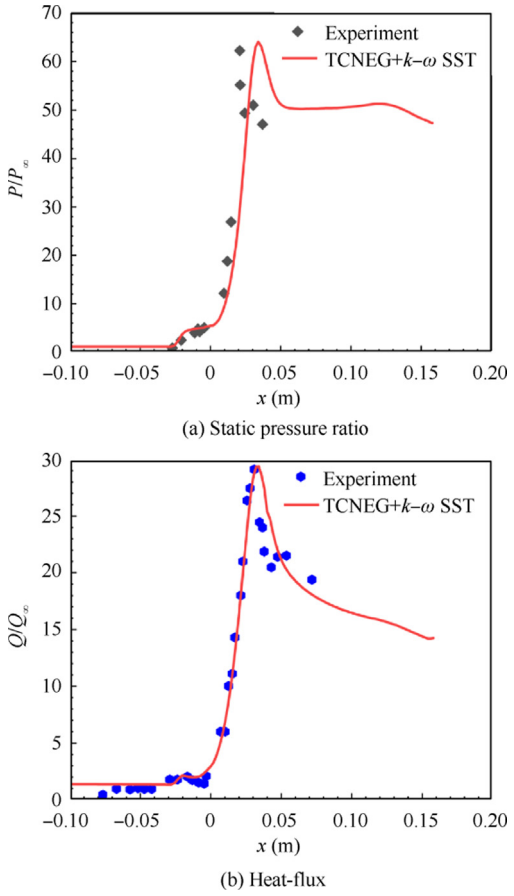

Fig. 8 Comparison between wall parameters from TCNEG coupling k-ω SST model and experimental results.[54]

gradually, which makes the effective capture mass flow of the inlet increase gradually; the cowl shock angle also decreases, the separation zone brought by the cowl shock/lower wall boundary layer interaction moves backward, and its scale becomes smaller. For Mach 8 and 9, there is an obvious separation zone upstream of the shoulder, and two shock reflections occur on the lower wall. For Mach 10, 11, and 12, the expansion wave at the shoulder weakens the cowl shock, causing that the separation zone is smaller than Mach 8 and 9, and there is only one shock reflection near the shoulder of the lower wall. Besides, the expansion wave at the shoulder strongly reflects on the upper wall.

To apprehend the influences of the thermochemical non-equilibrium effect on the flow separation, Fig. 11 displays the static pressure contours near the separation zone for different gas models at Mach 8. With the thermal process from frozen (TCFG) to non-equilibrium (TNCFG, TCNEG) and then to equilibrium (CNEG, TPG), the static temperature inside the flow field gradually decreases, and the boundary layer thins. Thus, the scales of separation bubbles are the thermal frozen gas (TCFG), thermal non-equilibrium gas (TNCFG, TCNEG), and thermal equilibrium gas (CNEG, TPG) from large to small. The intensity of the lower reflected shock for the thermal frozen gas is the strongest, and that for thermal equilibrium gas is the weakest, which causes that their performance parameters on the throat section differ greatly. Since the stagnation temperature at Mach 8 cannot fully activate the dissociation reactions of the molecule, the chemical reaction state can be regarded as frozen, and the separation bubble and shock structures at Mach 8 for TCNEG are the same as TNCFG, and these for CNEG are the same as those for TPG.

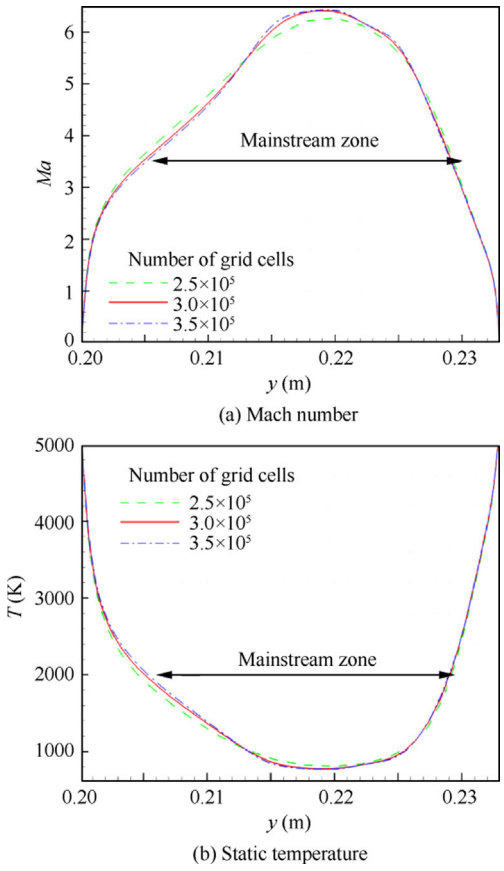

Fig. 9 Flow parameters at exit section calculated with three kinds of mesh.

From a macro perspective, the corresponding temperature change can express the energy transfer between translational-rotational and vibrational modes. Thus, similar to Ref. 34 and Ref. 58, the vibrational energy relaxation process can be well grasped employing the difference values ($T_{tr} - T_v$) between translational-rotational temperature T_{tr} and vibrational temperature T_v inside the inlet flow field which are presented in Fig. 12. The greater the absolute value of $T_{tr} - T_v$, the stronger the thermal non-equilibrium effect. At the external compression section, thermal non-equilibrium effects inside the boundary layer are stronger than those in the mainstream region. For the five working conditions at Mach 8 to 12, the static temperature behind the cowl shock increases, and the vibrational energy is excited, causing the thermal non-equilibrium effects significantly strengthen. In the zone near where the cowl shock/lower wall boundary layer interaction occurs, the thermal non-equilibrium effects are the strongest. As the vibrational temperature and flow time increase, the vibrational energy increases, so the thermal non-equilibrium effects inside the boundary layer near the lower wall weaken along the flow direction, downstream of the shoulder. With the increase of incoming Mach number, the flow velocity in the inlet channel increases and the flow characteristic time decreases, and the energy transfer amount from translational-rotational mode to vibrational mode decreases. Therefore, the absolute value of $T_{tr} - T_v$ increases, and the thermal non-equilibrium effects gradually strengthen. For Mach 10, 11, and 12, the static temperature decreases rapidly

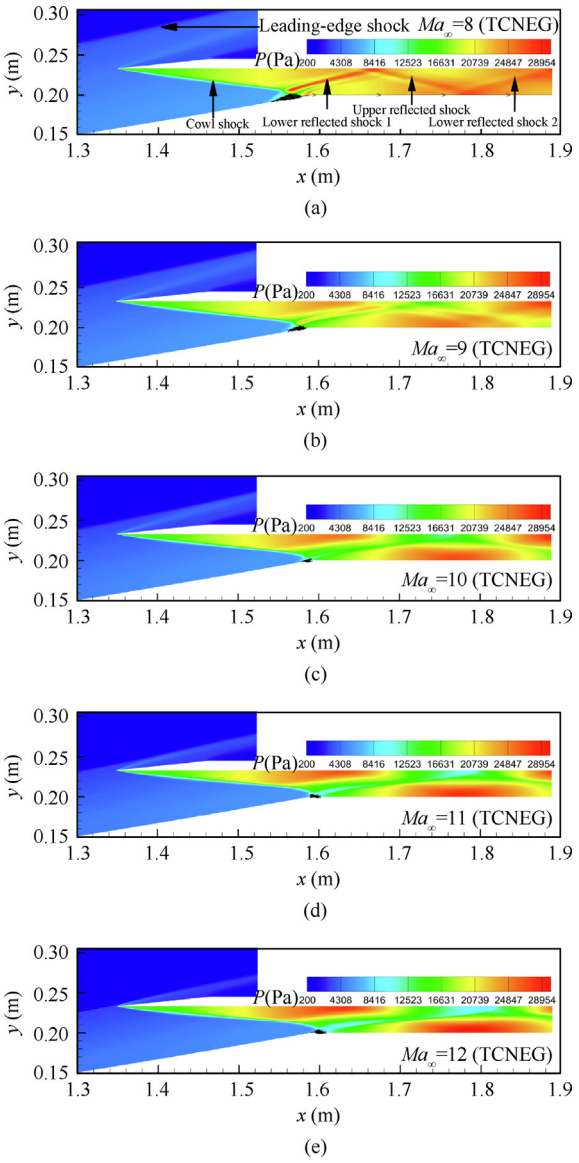

Fig. 10 Static pressure contours for TCNEG at different inflow Mach numbers: (a) Mach 8, (b) Mach 9, (c) Mach 10, (d) Mach 11, (e) Mach 12.

in the expansion zone near the upper wall (x = 1.7–1.8 m) and the lower wall (x = 1.8 m to the exit), yet the vibrational temperature decreases slowly. Thus the static temperature is lower than the vibrational temperature, which is called the vibrationally over-excited state. The locally enlarged views of Mach 10, 11, and 12 are visible in Fig. 13, the $T_{tr} - T_v < 0$ zone near the upper wall at Mach 12 is broader than that at Mach 10 and 11 due to its broader pressure expansion zone here.

4.2. Parameter analysis of wall, exit section, and center streamline in starting state

Fig. 14 reports the parameter distributions on the lower wall at Mach 8 to 12. From Fig. 14(a), the static temperature on the wall except near the leading edge changes little, which is close

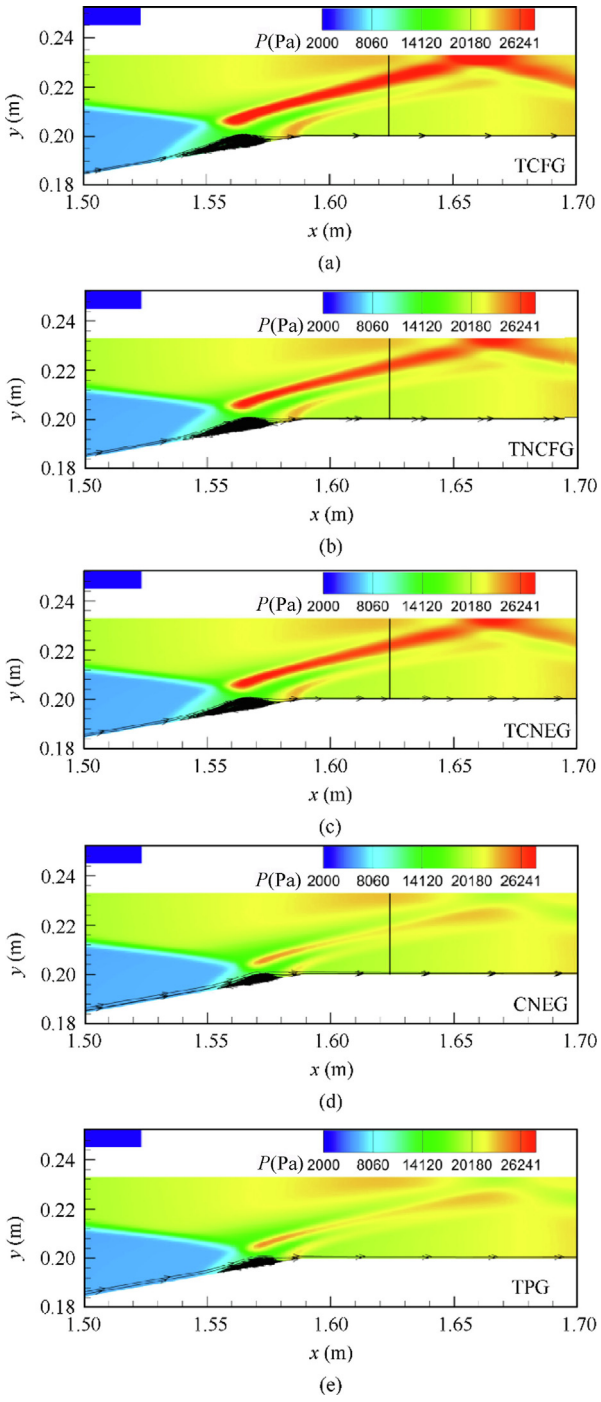

Fig. 11 Static pressure contours near separation zone at Mach 8: (a) TCFG, (b) TNCFG, (c) TCNEG, (d) CNEG, (e) TPG.

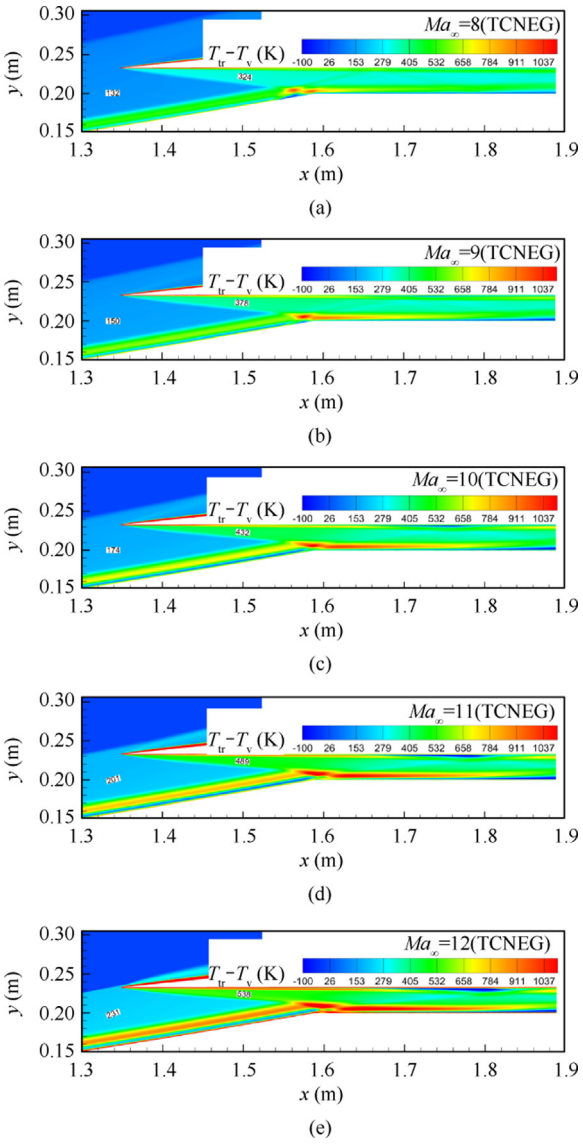

Fig. 12 $T_{tr} - T_v$ of inlet flow field at different inflow Mach numbers: (a) Mach 8, (b) Mach 9, (c) Mach 10, (d) Mach 11, (e) Mach 12.

to the stagnation temperature for each Mach number condition. However, the vibrational energy increases gradually with the flow, and the vibrational temperature on the wall increases at the external compression section, which can be seen in Fig. 14(b). Thus, thermal non-equilibrium effects on the wall gradually weaken along the flow direction, as exhibited in Fig. 14(c). At x = 0–0.4 m, thermal non-equilibrium effects of the wall at Mach 10, 11, and 12 are intenser than those at Mach 8 and 9, and the differences of $T_{tr} - T_v$ distribution become smaller with the increase of Mach number. Thermal non-equilibrium effects of the lower wall at Mach 12 are sharply more severe than the other four conditions from x = 0.4 m to the exit, and those distributions at Mach 8 and 9 are rather similar from x = 0.8 m to the exit.

The flow near the wall is in a stagnation state, static temperature here is the highest and close to stagnation temperature, indicating that the dissociation reactions near the wall are the most violent in the whole flow field. Fig. 14(d) displays oxygen mass fraction distributions near the lower wall at Mach 8 to 12. The oxygen mass fractions on the wall remain unchanged at 0.23 when the free stream flows at Mach 8 and 9, and the dissociation temperature of nitrogen is much higher than that of oxygen, indicating that no chemical reactions occur on the wall under the two working conditions. The oxygen mass fraction on the wall behind the shoulder

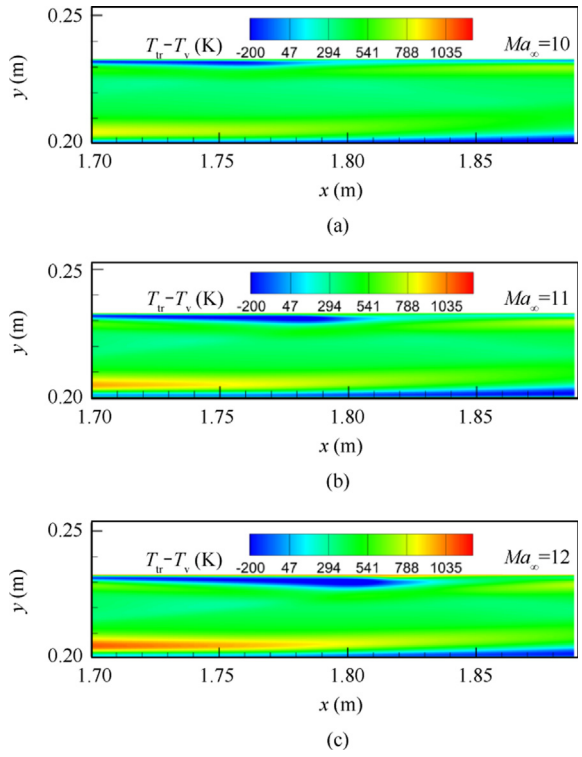

Fig. 13 Local enlarged views of (a) Mach 10, (b) Mach 11, (c) Mach 12 in Fig. 12.

decreases slightly at Mach 10, and the oxygen dissociation degree (ratio of consumption to its initial quantity) is relatively low, about 0.87%. The oxygen contents of Mach 11 and 12 start to decrease from the external compression section, those in the initial position of the separation bubble are the lowest due to the most violent dissociation reactions here, and the maximum dissociation degrees of the two are about 8.70% and 26.09%, respectively. The oxygen dissociation reactions at Mach 11 and 12 are more severe than those under the other three conditions.

As shown in Fig. 15(a), from $x = 1.4$ m to the exit, thermal non-equilibrium effects of the upper wall at Mach 12 are the most severe; those at Mach 8 to 10 are relatively similar and weaker than Mach 11 and 12. In Fig. 15(b), the oxygen mass fraction on the upper wall at Mach 8 to 9 cannot change along the flow direction, showing that there is no dissociation reaction of oxygen. The maximum dissociation degree of oxygen at Mach 10 is about 1.04%, and the oxygen dissociation reaction is weak. At Mach 11 and 12, the strong expansion waves are reflected near $x = 1.8$ m, and the static temperature and the static pressure can decrease; hence, the value of $T_{tr} - T_v$ can decrease, and the oxygen content can increase (because the reduction of static temperature promotes the compound reaction of oxygen). The maximum dissociation degrees of oxygen at Mach 11 and 12 are about 8.09% and 23.61%, respectively.

Fig. 16 presents the $T_{tr} - T_v$ and oxygen mass fraction distributions on the exit section at Mach 8 to 12. From Fig. 16(a), the $T_{tr} - T_v$ values are less than 0 K near the lower wall owing to expansion waves, but those are far greater than 0 K on the lower wall due to the stagnation flow. In the mainstream zone, the $T_{tr} - T_v$ values of all Mach numbers are more than 300 K, implying that thermal non-equilibrium effects are relatively strong. As Fig. 16(b) displays, oxygen mass fractions of Mach 10, 11, and 12 gradually decrease in the zone from $x = 0.215$ m to the lower wall and from $x = 0.223$ m to the upper wall. And it can be seen that oxygen dissociation reaction occurs in most areas of the exit section. From Fig. 10, at Mach 10, 11, and 12, shock wave and expansion wave reflections occur on the upper and lower wall near the exit section, respectively, and the static temperature and static pressure rise caused by shock wave reflection can promote dissociation reactions. Thus, the oxygen content on the upper wall is more than that on the lower wall, which can be seen in Fig. 16(b).

Fig. 17 shows the parameter distributions of the mainstream center streamline at Mach 8 to 12, and the streamline position can be seen in Appendix B. Fig. B1 presents the central streamline and Mach number contours inside thermochemical non-equilibrium flow field at Mach 12. From Fig. 17(a), the static temperature T increases markedly after the leading-edge curved shock compression and then increases nearly linearly, and the T maximum values for all Mach conditions are lower than 500 K at the external compression section, implying that the molecule vibration energy of the mainstream zone cannot be excited (in frozen state) here. T increases sharply after the cowl shock compression, T of Mach 12 and 8 increase to about 860 K and 570 K, respectively. And then, the T drops of all Mach conditions are noted, which is caused by an expansion wave domain formed by the shoulder. Since the shock reflection phenomena exist in the internal compression section, T distributions downstream of the cowl shock oscillate for each Mach condition.

Unlike the T distribution, after the leading-edge curved shock compression, the vibrational temperature T_v is the same as the incoming T_v and invariant at the external compression section, which can be observed in Fig. 17(b). The variation trend of T_v expresses again that the mainstream flows at the external compression section are in thermal frozen state for each Mach number. Downstream of the cowl shock, T_v starts to increase continuously due to the excitation of the vibrational energy, but T_v distribution for each Mach number does not oscillate due to the slow relaxation processes of the vibration energy. Notably, the vibrational energy can be further excited after the reflected shock, so the growth slopes of T_v increase. In the whole, the change amplitude of T_v after the reflected shock is smaller than that of T. As the incoming Mach number increases, more and more vibration energy excitation causes that T_v increases faster and faster. From the cowl shock to the exit, T_v of Mach 12 and 8 increase by about 80.1% and 19.8%, respectively.

As displayed in Fig. 17(c), though the $T_{tr} - T_v$ values of the external compression section are positive, the flows remain in thermal frozen state since no vibration energy of the mainstream zone is excited. The thermal or vibrational non-equilibrium effects sharply become violent after the cowl shock compression, which can also be observed in Fig. 12. With the increase of incoming Mach number, the vibrational non-equilibrium effects downstream of the cowl shock gradually strengthen. From Fig. 17(d), the $T_{tr} - T_v$ values of Mach 12 and 11 immediately reach the peak after the cowl shock compression, yet those of Mach 10 and 9 after the cowl shock slowly increase to the peak. It is after the first reflected shock on the lower wall that the $T_{tr} - T_v$ value of Mach 8 reaches the peak. The $T_{tr} - T_v$ values of Mach 12, 11, and 10 drop signif-

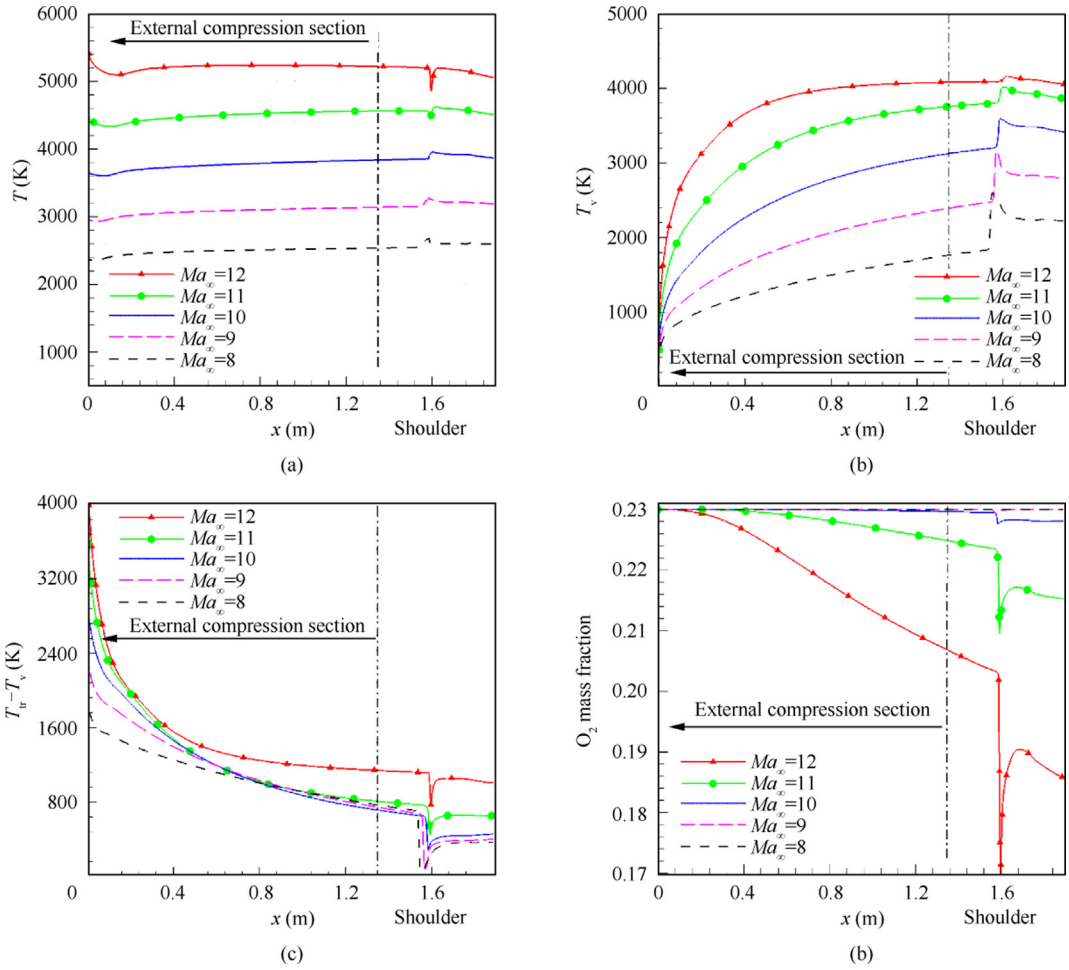

Fig. 14 Parameter distributions on lower wall at Mach 8 to 12: (a) Static temperature, (b) Vibrational temperature, (c) $T_{tr} - T_v$, (d) Oxygen mass fraction.

icantly after the peak due to the broad expansion area, and they change within a large range since the shock wave and expansion wave are relatively stronger than Mach 8 and 9. Significantly, at $x = 1.888$ m, the $T_{tr} - T_v$ values of the five Mach numbers are in the range from 320 K to 370 K, indicating that the thermal non-equilibrium effects at the exit section still are intense and certainly spread to the combustor.

From the above analysis, there is no dissociation reaction of oxygen on the wall for Mach 8 and 9, and the dissociation temperature of nitrogen is higher than that of oxygen, so the chemical reactions are frozen in the inlet flow field for Mach 8 and 9. The oxygen dissociation reaction at Mach 10 is weak, and those at Mach 11 and Mach 12 are strong. Hence, we can consider that except for the mainstream region upstream of the cowl shock, the inlet flows at Mach 8 and 9 are in a thermal out-of-equilibrium and chemical frozen status, but those at Mach 10, 11, and 12 are in a thermal and chemical non-equilibrium status.

4.3. Analysis of inlet performance parameters in starting state

Fig. 18 exhibits throat performance parameters of different thermochemical gas models in the wide Mach range, and each parameter is calculated by a mass-weighted average method. T/T_∞, P/P_∞, Ma, and σ ($P_{total}/P_{total,\infty}$) respectively denote the static temperature ratio, static pressure ratio, Mach number, and total pressure recovery coefficient, and the subscript "th" indicates the throat section.

In Fig. 18(a), as the thermal state changes from frozen (TCFG) to non-equilibrium (TCNEG and TNCFG) and then to equilibrium (CNEG and TPG), more translational-rotational energies are transferred to the vibrational energy mode, which makes the translational-rotational or static temperature in the flow field gradually decrease, so the T_{th}/T_∞ gradually decreases. For Mach 8, 9, and 10, the chemical reaction statuses which are close to being frozen have little effect on the static temperature of the throat section; therefore, T_{th}/T_∞ of TCNEG and TNCFG are the same, and T_{th}/T_∞ of CNEG and TPG are almost consistent. For Mach 12, the endothermic dissociation reactions make T_{th}/T_∞ of TCNEG be about 1.32% lower than that of TNCFG, and T_{th}/T_∞ of CNEG be about 1.35% lower than that of TPG. From Fig. 18(b), with the increase of incoming Mach number, the distinctions among P_{th}/P_∞ of different thermochemical models become smaller. The reason for the above trend should be that the size of the separation zone and the shock reflection are easily susceptible to thermochemical non-equilibrium effects at Mach 8 (discussed in Fig. 11), yet hard to change at Mach

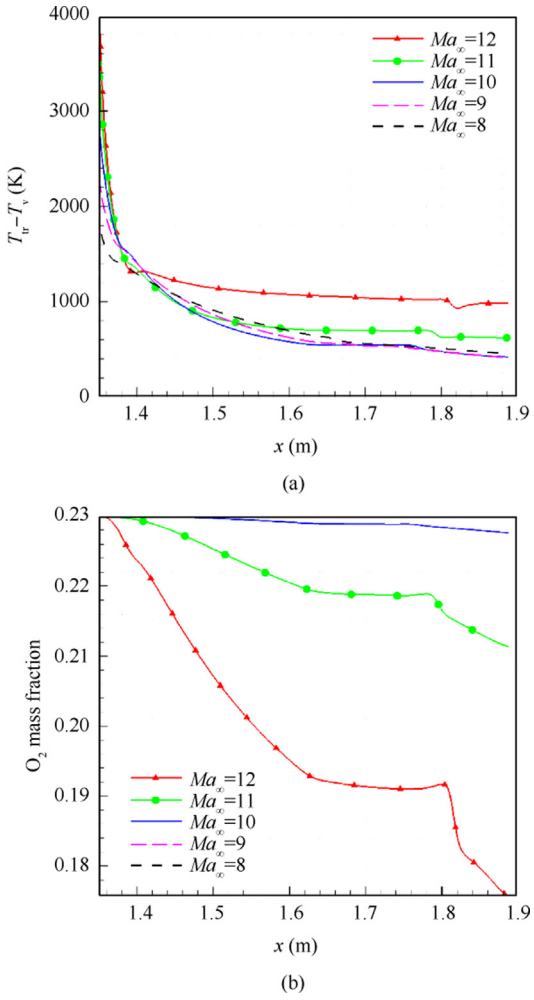

Fig. 15 Parameter distributions on upper wall at Mach 8 to 12: (a) $T_{tr} - T_v$, (b) Oxygen mass fraction.

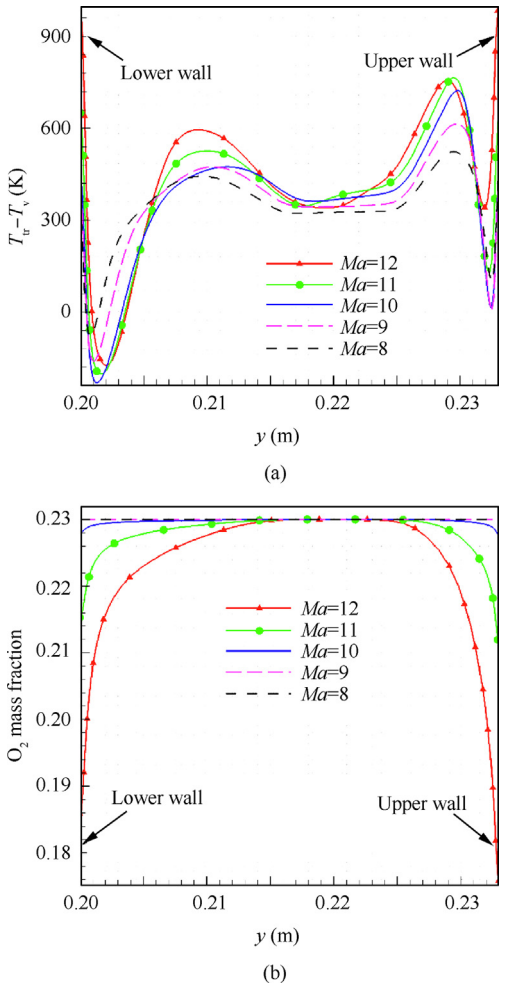

Fig. 16 Parameter distribution on exit section at Mach 8 to 12: (a) $T_{tr} - T_v$, (b) Oxygen mass fraction.

11 and 12 due to the smaller separation bubble. At Mach 8, P_{th}/P_∞ of thermal non-equilibrium models (TCNEG and TNCFG) is about 2.55% lower than that of thermal frozen model (TCFG), and 5.5% higher than that of thermal equilibrium models (CNEG and TPG). If the static temperature is lower, the value of the specific heat ratio and sound speed are smaller; the shock wave is weaker, and the boundary layer is thinner, which can help to reduce total pressure loss. Thus, the Ma_{th} and σ_{th} values of TCNEG and TNCFG are higher than those of TCFG and lower than those of CNEG and TPG, which is exhibited in Figs. 18(c) and (d).

The exit performance parameters of different thermochemical gas models in the wide Mach range are presented in Fig. 19, and the subscript "exit" denotes the exit section. From Fig. 19(a), we can see that at Mach 8, 9, and 10, the chemical reaction still cannot change the exit static temperature in the same thermal state. For Mach 8 and 12, T_{exit}/T_∞ of TCNEG are 5.64% and 9.52% respectively, lower than those of TCFG. But T_{th}/T_∞ of TCNEG separately are 1.91% and 2.76% lower than TCFG (Fig. 18(a)), meaning that the difference between the static temperature of TCNEG and TCFG is gradually amplified with the flow (from throat to exit section). Moreover, the dissociation reaction at the exit section is stronger than that at the throat section, so T_{exit}/T_∞ of TCNEG is 2.58% lower than that of TNCFG for Mach 12, and the disparity here is larger than that at the throat section.

As reported in Fig. 19(b), since shock reflections in the isolator are vulnerable to thermochemical non-equilibrium effects[24] and the static pressure distribution mainly depends on wave structures in the flow field, the differences in static pressure among different thermochemical models at exit section are more significant than those at throat section, for Mach 10, 11, and 12. At Mach 10, P_{exit}/P_∞ of TCNEG is 4.92% lower than that of TCFG, and 5.64% higher than that of CNEG; at Mach 12, P_{exit}/P_∞ of TCNEG is 11.84% lower than that of TCFG, and 3.78% higher than that of CNEG.

As exhibited in Fig. 19(c), for Mach 8, Ma_{exit} of TCNEG is 1.67% higher than that of TCFG, and 3.05% lower than that of CNEG; for Mach 12, Ma_{exit} of TCNEG is 5.44% higher than that of TCFG, and 3.53% lower than that of CNEG. The chemical reaction cannot significantly change the exit Mach number in the same thermal state as well. From Fig. 19(d), we can see that at Mach 10, 11, and 12, σ_{exit} values of thermal non-equilibrium gases (TCNEG and TCFG) are near to those of thermal equilibrium gases (CNEG and TPG) rather than thermal frozen gas (TCFG), which is unlike

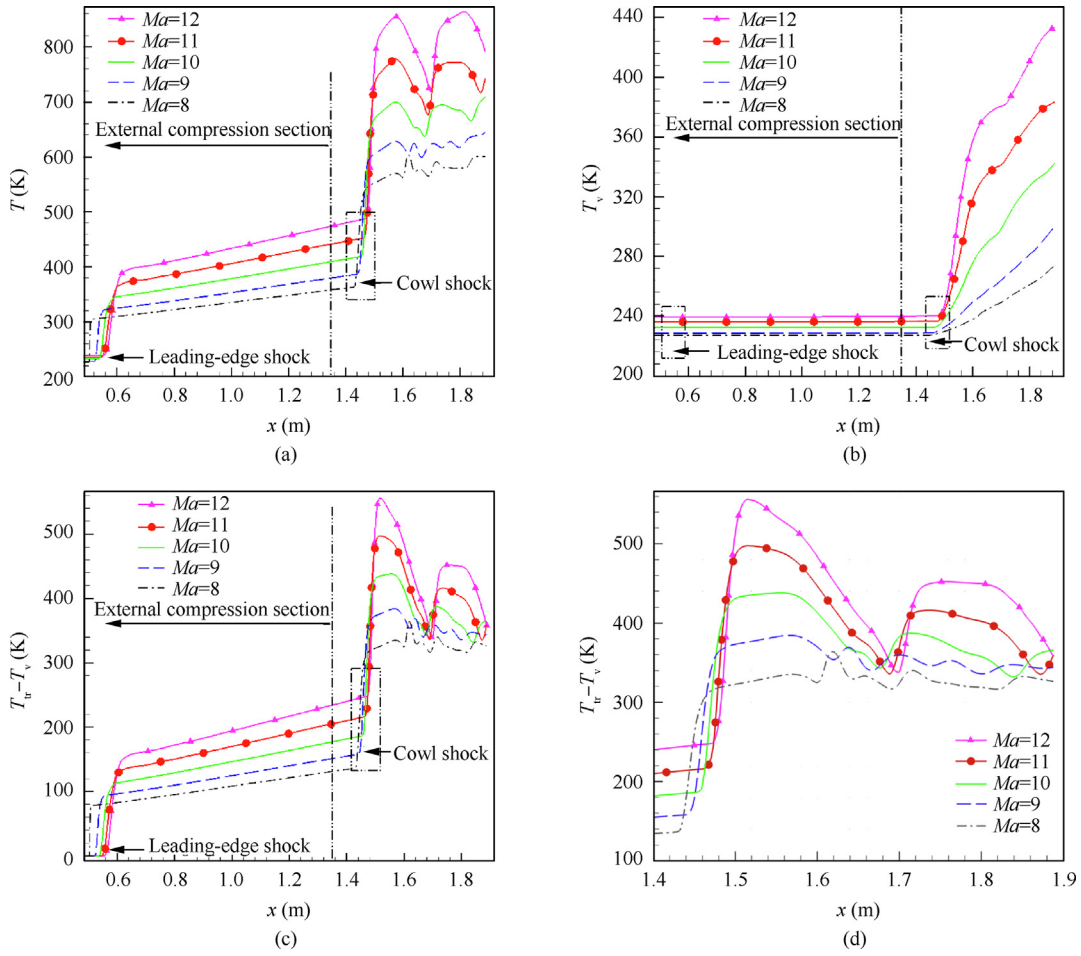

Fig. 17 Parameter distribution of mainstream center streamline at Mach 8 to 12: (a) Static temperature, (b) Vibrational temperature, (c) $T_{tr} - T_v$, (d) Enlarged view of $T_{tr} - T_v$.

the trend at throat section. The reason for the above distinction should be that the thermal state along the flow direction will tend to develop in equilibrium. With the increase of incoming Mach number, the disparity in mass flow coefficients (φ) among different thermochemical models becomes more noticeable, which can be seen in Fig. 19(e). At Mach 12, φ of TCNEG is 1.44% higher than TCFG, and 1.31% lower than CNEG, and these trends are decided by the leading-edge curved shock positions.

The thermochemical state directly affects the static temperature, and the specific heat directly influences the flow structures, thereby altering the static pressure distribution. In a word, at Mach 11 and 12, the dissociation reaction has a greater impact on the static temperature and pressure of the exit section. As the incoming Mach number increases, thermochemical non-equilibrium effects gradually intensify. Consequently, the performance parameter distributions (T/T_∞, Ma, and P/P_∞) of TCNEG gradually deviate from TCFG, and the overall work performance differences of different thermochemical models become larger. Significantly, compared with the chemical non-equilibrium reaction, the thermal state can produce greater influences on the inlet's overall performance.

4.4. Influence of thermochemical non-equilibrium effects on starting characteristics

Since whether an inlet can operate normally in a wide working range is directly determined by its starting and restarting capability, the influences of thermochemical non-equilibrium effects on the starting and restarting characteristics of the high Mach number inlet are investigated by simulating the reduction and increase processes of flight Mach number. The three thermochemical models of TCFG, TCNEG, and CNEG are employed for the numerical calculations in this section.

Taking the starting flow field of the inlet passage as the initial calculated flow field and keeping static pressure and static temperature of incoming flow unchanged, the lowest starting Mach number from the start state to the unstart one is obtained by reducing the flight Mach number. Fig. 20 presents the flow fields at low flight Mach number for different thermochemical gas models. As displayed in Figs. 20(a), (c), and (e), at Mach 3.7, the cowl shock interacts with the lower wall boundary layer to form a typical flow separation structure such as the separation shock, separation bubble, and reattached shock. In addition, the flows in the entire channel are supersonic, and the shock wave structures in the flow field have

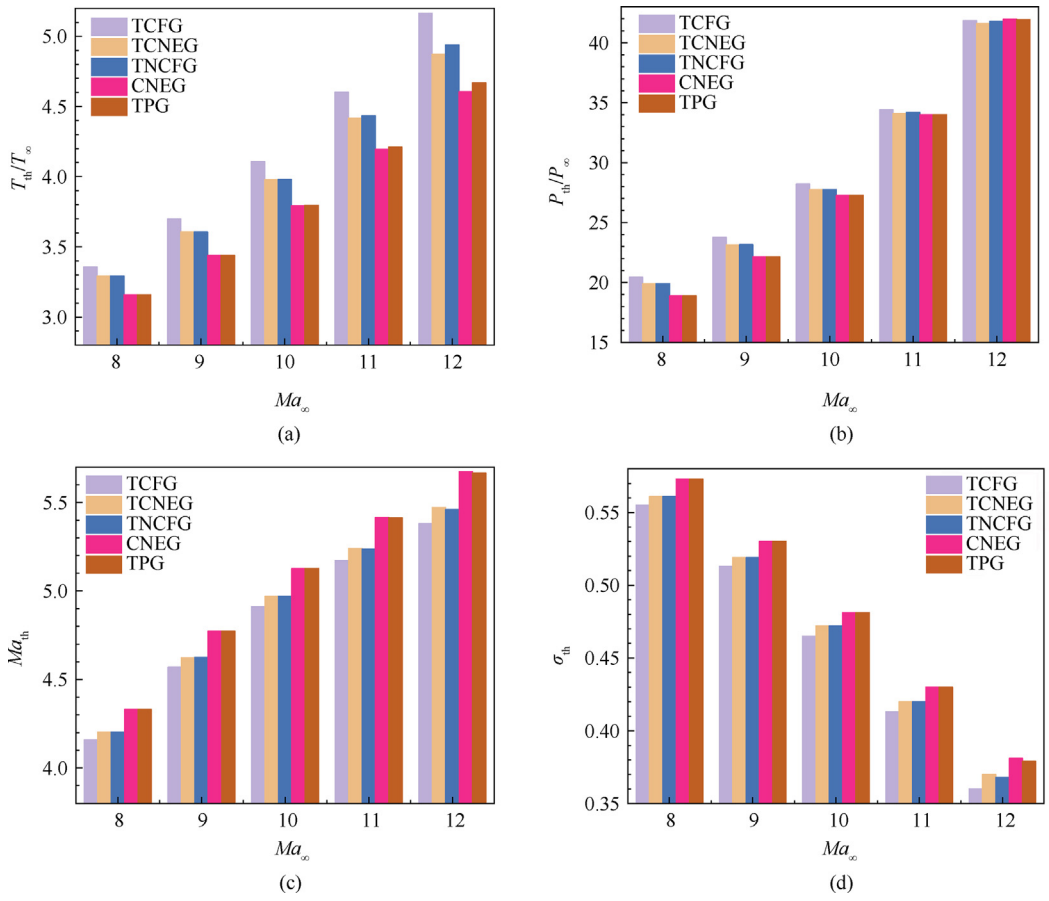

Fig. 18 Throat performance of different thermochemical gas models in wide Mach range: (a) Static temperature ratio, (b) Static pressure ratio, (c) Mach number, (d) Total pressure recovery coefficient.

been established normally, so the inlet at Mach 3.7 is regarded as being in starting condition. Nevertheless, at Mach 3.6, the large separation bubbles occur near the cowl and cause the flow choking in the whole channel, which is revealed in Figs. 20(b), (d), and (f). Thus, we argue that the inlet fails to start normally at Mach 3.6. The thermochemical non-equilibrium effects are extremely weak at Mach 3.6 and 3.7, and their influence can be ignored. Consequently, the start and unstart flow fields of the three thermochemical models are the same at low flight Mach numbers.

Based on Ref. 59, although the restarting process of the supersonic and hypersonic inlet is unsteady, the influence of the unsteady effects caused by its acceleration magnitude on the restarting characteristics of the inlet is not obvious. Moreover, Wu et al.[60] investigated the restarting process of a hypersonic inlet with the variable incoming conditions by the quasi-steady and unsteady two-dimensional numerical calculations. It can be found that the restarting Mach numbers of the inlet obtained by the two methods are the same, and the quasi-steady method can largely improve simulation efficiency. Regretfully, the unsteady effects during the inlet restarting process are not the focus of this study, yet will be carefully explored in future work. This paper focuses on the inlet restarting Mach number in thermochemical non-equilibrium flows. Therefore, a quasi-steady simulation method is utilized to predict the inlet restarting characteristics, and the specific details are as follows: the convergence result of the unstart flow field at Mach 3.6 is employed to initialize the quasi-steady calculation, and the flight Mach number is gradually increased at the interval of Mach 0.1 for further calculation. Then, the restarting Mach number cannot be obtained until the starting flow field is established. Moreover, the above quasi-steady method has been successfully applied to estimating the restarting performance of the mixed compression inlet[4,61,62].

Fig. 21 presents the flow structures for different gas models at Mach 8.0 during the restarting process, the white solid line inside the flow field denotes the sound speed line, and LECS here represents the Leading-Edge Curved Shock formed by curved compression surface. First, taking the flow field for TCFG as an example, in Fig. 21(a), a large separation zone SZ1 is located below the cowl and almost occupies the whole channel, so the inlet also unstarts. The separation shock SS formed by SZ1 does not intersect the cowl, and the reattached shock RS1 brought by SZ1 interacts with the upper wall boundary layer to cause the separation zone SZ2. Then, the separation zone SZ3 is induced by the interaction of the reattached shock RS2 and the lower wall boundary layer. The higher the static temperature, the larger the separation region[63]. The static temperature inside the flow field for TCNEG is lower than that for TCFG, but higher than that for CNEG, so the SZ1 and SZ2 sizes for TCNEG are smaller than TCFG and yet larger than CNEG, which is visible in Fig. 21(b). Compared with TCNEG, the SS position for

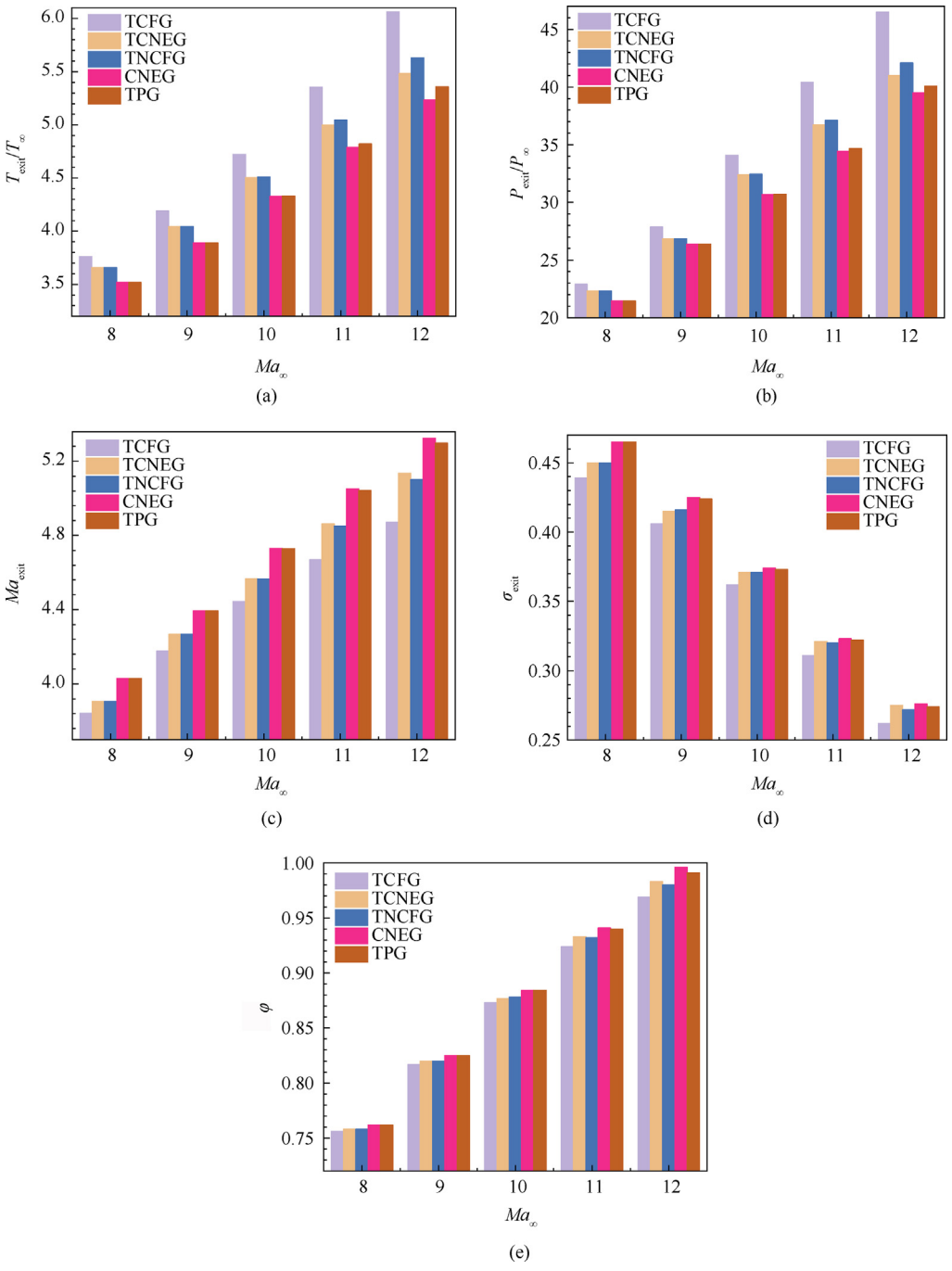

Fig. 19 Exit performance of different thermochemical gas models in wide Mach range: (a) Static temperature ratio, (b) Static pressure ratio, (c) Mach number, (d) Total pressure recovery coefficient (e) Mass flow coefficient.

TCFG is closer to upstream, and that for CNEG is closer to downstream (Fig. 21(c)).

Fig. 22 reveals the flow structures for different gas models at Mach 8.2 during the restarting process. In Fig. 22(a), the separation zones and shock structures for TCFG at Mach 8.2 are very similar to those at Mach 8.0. From Fig. 22(b), compared with Mach 8.0, the SZ1 size for TCNEG at Mach 8.2 is smaller, and its SS is closer downstream, but SZ2 has little change. As represented in Fig. 22(c), for CNEG, the large separation zone SZ1 below the cowl disappears at Mach 8.2, and there is a small separation zone upstream of the shoulder point, but the entire channel flows are supersonic (the inlet is normally starting). Therefore, we judge that the inlet for CNEG can restart at Mach 8.2, while the inlets for TCFG and TCNEG still unstart and cannot restart.

Fig. 23 presents the flow structures for different gas models at Mach 8.8 during the restarting process, and the flow filed for CNEG needs not be given and discussed here because the inlet for it has achieved restarting status at Mach 8.2. From Fig. 23(a), the unstart flow structures for TCFG at Mach 8.8 have no significant difference from those at Mach 8.0 and 8.2. However, the wave systems inside the TCNEG flow field

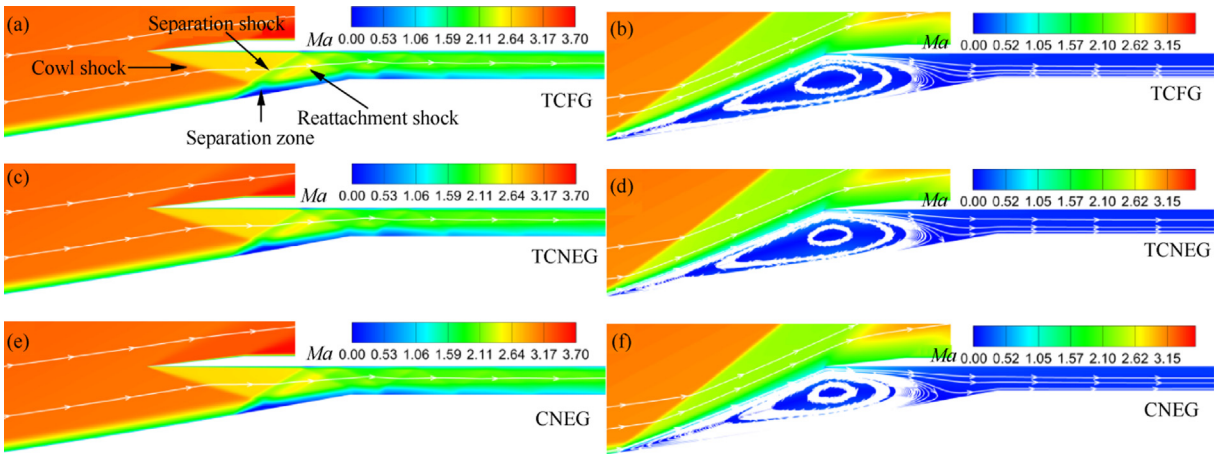

Fig. 20 Flow fields at low flight Mach number for different thermochemical gas models: (a) Mach 3.7, TCFG, (b) Mach 3.6, TCFG, (c) Mach 3.7, TCNEG, (d) Mach 3.6, TCNEG, (e) Mach 3.7, CNEG, (f) Mach 3.6, CNEG.

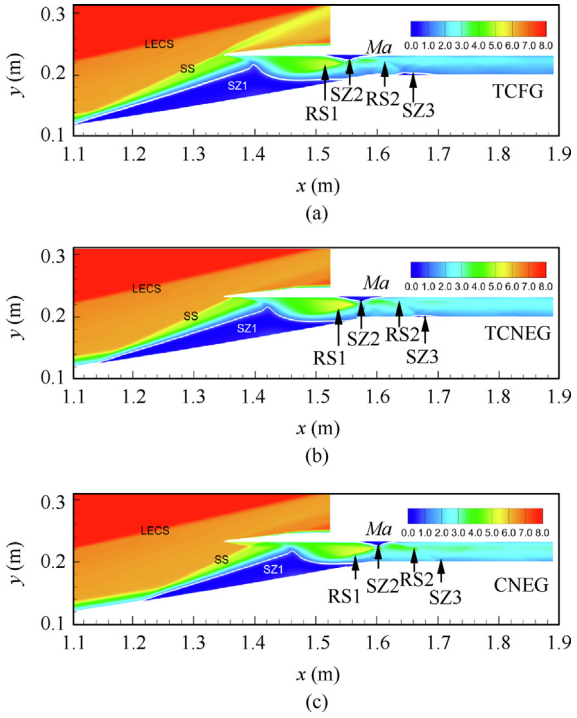

Fig. 21 Flow structures for different gas models at Mach 8.0 during restarting process: (a) TCFG, (b) TCNEG, (c) CNEG.

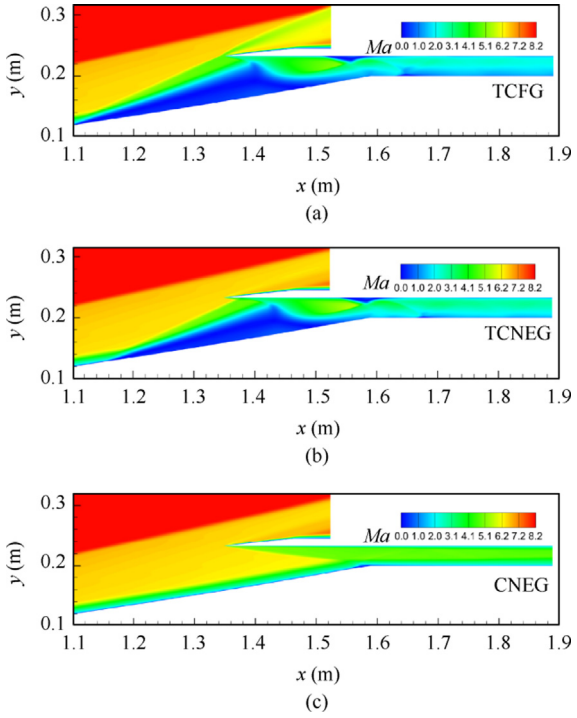

Fig. 22 Flow structures for different gas models at Mach 8.2 during restarting process: (a) TCFG, (b) TCNEG, (c) CNEG.

are well structured at Mach 8.8, and the inlet can restart under this Mach condition, which is shown in Fig. 23(b).

Since the inlet restarting Mach numbers for TCNEG and CNEG are Mach 8.8 and 8.2, respectively, the flow fields for these two gas models above Mach 8.8 are no longer concerned. Fig. 24 reveals the flow structures for TCFG at Mach 10 and 12 during the restarting process. As flight Mach number increases (from Mach 8.0 to 12), the angle of SS decreases gradually. Yet, the starting location of the SZ1 moves forward and its area expands, which is contrary to the changing trend of the other two gas models (TCNEG and CNEG). Unfortunately, the inlet for TCFG still does not start under design condition (Mach 12), which is exhibited in Fig. 24(b). The calculation cases for TCFG are mainly applied to the comparative analyses, so its specific restarting Mach number will not be sought here. From the above results, it can be found that there is a great difference in the inlet restarting capabilities among different thermochemical gas models.

Overall, since high-temperature effects may not occur at low flight Mach numbers, the lowest starting Mach numbers for all the three thermochemical models are Mach 3.7. However, the high-temperature effects will become severe in the

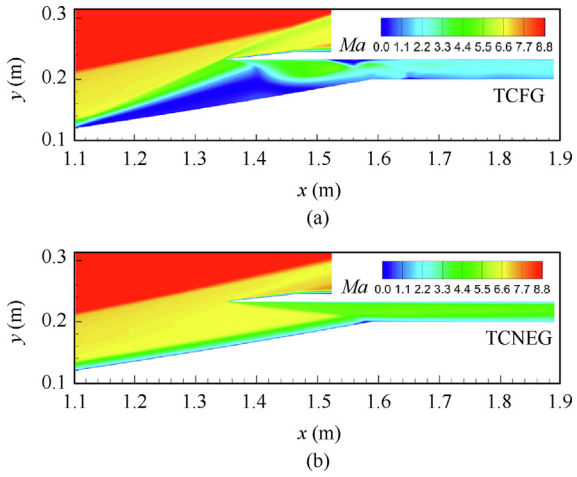

Fig. 23 Flow structures for different gas models at Mach 8.8 during restarting process: (a) TCFG, (b) TCNEG.

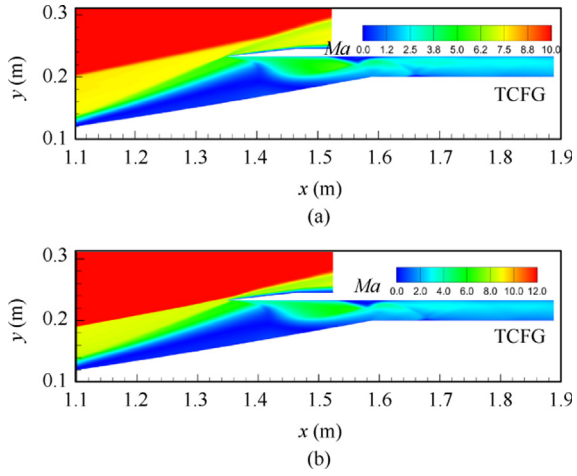

Fig. 24 Flow structures for TCFG at Mach 10 and 12 during restarting process: (a) Mach 10, (b) Mach 12.

process of finding the restarting Mach number, so thermochemical non-equilibrium effects may affect the inlet restarting ability. As the thermal state changes from frozen to non-equilibrium and then to equilibrium, the static temperature decreases (Fig. 25), the viscosity decreases, and the density increases (due to the static pressure independent of variable thermal states). Then, the boundary layer becomes thinner and the flow speed can increase (Fig. 25), which contributes to the restarting of the inlet. Therefore, the inlet in the TCNEG flows is easier to restart than that in the TCFG flows, but harder to restart than that in the CNEG flows.

The main separation zone (SZ1) below the cowl is an important feature of the inlet unstart state, and the thickness of the boundary layer upstream of the main separation zone is the key to determining whether the main separation zone can exist stably. From the current preliminary research, we infer that the high-temperature effects can change the thickness of the boundary layer upstream of the separation zone below the cowl, and then affect the restart performance of the high Mach number inlet.

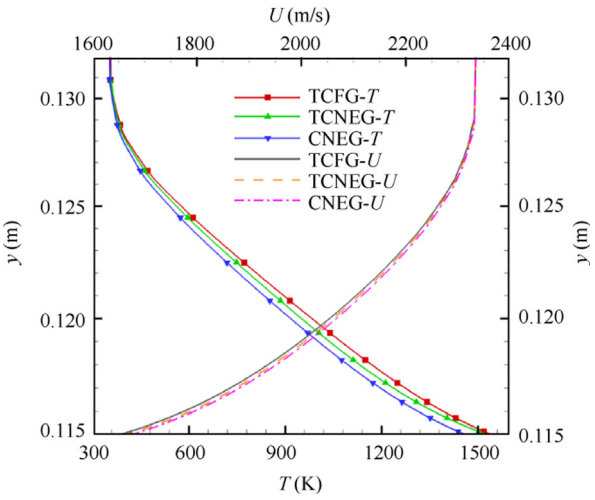

Fig. 25 Static temperature and x-axis velocity inside boundary layer upstream of separation zone.

5. Conclusions

In the present work, we numerically investigate the thermochemical non-equilibrium flows of a high Mach number two-dimensional inlet in the wide work range by employing the two-dimensional RANS solver. The high enthalpy double cone and high Mach number compression corner experiments are utilized for testing the prediction ability of the current solvers in high Mach number thermochemical non-equilibrium turbulence flows. The thermochemical non-equilibrium flows and working performance of the inlet at Mach 8 to 12 are discussed, and then the influences of thermochemical non-equilibrium effects on the inlet starting characteristics are analyzed. The vital conclusions are presented in the following:

(1) At Mach 8 and 9, the obvious separation zones caused by the cowl shock/lower wall boundary layer interaction are upstream of the shoulder. The separation zone size of the thermal non-equilibrium model is smaller than that of the thermal frozen model, but larger than that of the thermal equilibrium model.
(2) The flows inside the boundary layer and near the wall are all in the thermal out-of-equilibrium status, and the vibrational energy in the mainstream zone can be excited after the cowl shock compression. As flight Mach number increases, thermal non-equilibrium effects in the whole inlet flow field gradually strengthen.
(3) After the shock reflections, the static temperature in the mainstream zone distribution fluctuates greatly, yet the growth slopes of the vibrational temperature increase. At Mach 10 to 12, the vibrationally over-excited phenomenon occurs in the expansion area of the internal compression section. The chemical reaction processes in the flow field are frozen at Mach 8, 9, and 10, yet those are in non-equilibrium at Mach 11 and 12.
(4) As the flight Mach number increases, the influences of thermal non-equilibrium effects on the inlet performance parameters become more obvious. The chemical non-equilibrium reactions only affect the inlet exit performance at Mach 11 and 12. Compared with chemical

non-equilibrium effects, the thermal non-equilibrium effects have some larger impacts on the inlet work performance.

(5) The high-temperature non-equilibrium effects do not change the minimum starting Mach number of the inlet; however, these may seriously affect the inlet restarting ability. The inlet for thermochemical non-equilibrium gas can restart more easily than that in the thermochemical frozen flow, but more arduously than that in the chemical non-equilibrium flow.

Declaration of Competing Interest

The authors declare that they have no known competing financial interests or personal relationships that could have appeared to influence the work reported in this paper.

Acknowledgements

This study was co-supported by the China Scholarship Council (No. 202206840048), the Training Fund for Excellent Doctoral Candidates of Nanjing University of Science and Technology, China, the Opening Foundation of State Key Laboratory of High Temperature Gas Dynamics, Institute of Mechanics, China (No. 2021KF07), the National Key Laboratory Fund, China (No. 2022-JCJQ-LB-020-01), the Foundation of Key Laboratory of Hypersonic Aerodynamic Force and Heat Technology, AVIC Aerodynamics Research Institute, China (No. XFX20220104), the China Postdoctoral Science Foundation (No. BX20200070), and the Fundamental Research Foundation of the Central Universities, China (No. 2022CDJXY-012).

Appendix A. Transport coefficients & turbulence model

Unlike general supersonic flows, the influence of high-temperature effects on gas transport characteristics such as viscosity, thermal conduction, and mass diffusion should be taken seriously in high Mach number turbulence flows. Hence, a transport model suitable for high-temperature flows should be applied to all current numerical simulations, rather than the Sutherland model[44] frequently employed in modeling supersonic turbulence flows.[45,46] The Gupta-Yos's transport model (Eqs. (A1) and (A2)) is employed, and the values of all constant coefficients here are the same as those in Ref. 48. The mixture transport properties are computed by adopting the mixing law of Wilke.[47]

$$\ln \mu_s = A_{\mu,s}(\ln T)^4 + B_{\mu,s}(\ln T)^3 + C_{\mu,s}(\ln T)^2 + D_{\mu,s}\ln T + E_{\mu,s} \tag{A1}$$

$$\ln \lambda_s = A_{\lambda,s}(\ln T)^4 + B_{\lambda,s}(\ln T)^3 + C_{\lambda,s}(\ln T)^2 + D_{\lambda,s}\ln T + E_{\lambda,s} \tag{A2}$$

The turbulent viscosity coefficient μ_T is computed through solving turbulence equations. The turbulent thermal conductivities are equal to $\lambda_{tr,T} = C_{p,tr}(\mu_T/Pr_T)$, $\lambda_{v,T} = C_{p,v}(\mu_T/Pr_T)$, C_p denotes the specific heat at constant pressure, and the turbulent Prandtl number Pr_T is equivalent to 0.9. The diffusion coefficient can be described as $D = [\mu_L/(\rho \cdot Sc_L)] + [\mu_T/(\rho \cdot Sc_T)]$, and the laminar and turbulent Schmidt numbers (Sc_L and Sc_T) are set as 0.525 and 0.7, respectively.

The basic equations of the k-ω SST turbulence model[42] are expressed as

$$\frac{\partial \rho k}{\partial t} + \frac{\partial(\rho u_i k)}{\partial x_i} = \widetilde{P}_k - \beta^* \rho k\omega + \frac{\partial}{\partial x_i}\left[(\mu_L + \sigma_k \mu_T)\frac{\partial k}{\partial x_i}\right] \tag{A3}$$

$$\frac{\partial \rho \omega}{\partial t} + \frac{\partial(\rho u_i \omega)}{\partial x_i} = \frac{\gamma}{\nu_T} P_k - \beta \rho \omega^2 + \frac{\partial}{\partial x_i}\left[(\mu_L + \sigma_\omega \mu_T)\frac{\partial \omega}{\partial x_i}\right] + 2\rho(1 - F_1)\frac{\sigma_{\omega 2}}{\omega}\cdot\frac{\partial k}{\partial x_i}\cdot\frac{\partial \omega}{\partial x_i} \tag{A4}$$

here, P_k and F_1 denote the turbulence generation term and transformed function, respectively, and they are defined as

$$P_k = \left[\mu_T\left(\frac{\partial u_i}{\partial x_j} + \frac{\partial u_j}{\partial x_i} + \frac{2}{3}\cdot\frac{\partial u_k}{\partial x_k}\cdot\delta_{ij}\right) - \frac{2}{3}\rho k \delta_{ij}\right]\frac{\partial u_i}{\partial x_j}$$
$$\widetilde{P_k} = \min(P_k,\ 10\beta^* \rho k\omega) \tag{A5}$$

$$F_1 = \tanh\left\{\left\{\min\left[\max\left(\frac{\sqrt{k}}{\beta\omega d}, \frac{500\nu}{d^2\omega}\right), \frac{4\rho\sigma_{\omega 2}k}{\mathrm{CD}_{k\omega}d^2}\right]\right\}^4\right\} \tag{A6}$$

$$\mathrm{CD}_{k\omega} = \max\left(2\rho\sigma_{\omega 2}\frac{1}{\omega}\cdot\frac{\partial k}{\partial x_j}\cdot\frac{\partial \omega}{\partial x_j}, 10^{-20}\right) \tag{A7}$$

where d denotes the nearest distance to the wall. Wilcox's k-ω model can be activated in the viscous sublayer zone when $F_1 = 1$, but standard k-ε model is activated in the area away from the wall when $F_1 = 0$. In the ω Eq. (A4), the turbulent eddy viscosity ν_T is given as

$$\nu_T = \frac{a_1 k}{\max\{a_1\omega, SF_2\}}$$
$$F_2 = \tanh\left\{\left[\max\left(\frac{2\sqrt{k}}{\beta^*\omega d}, \frac{500\nu}{d^2\omega}\right)\right]^2\right\} \tag{A8}$$

From the corresponding constants in Wilcox's k-ω and standard k-ε models, a blend form $\phi = \phi_1 F_1 + \phi_2(1 - F_1)$ is employed to compute all constants in k-ω SST model, where $\beta^* = 0.09$, $a_1 = 0.31$, $k = 0.41$, $\gamma_1 = 0.553$, $\beta_1 = 0.075$, $\sigma_{k1} = 0.85$, $\sigma_{\omega 1} = 0.5$, $\gamma_2 = 0.44$, $\beta_2 = 0.0828$, $\sigma_{k2} = 1.0$, $\sigma_{\omega 2} = 0.856$.

Appendix B. Mainstream center streamline position

As displayed in Fig. B1, the mainstream center streamline passes through the point of $(x, y) = (0, 0.1)$ m.

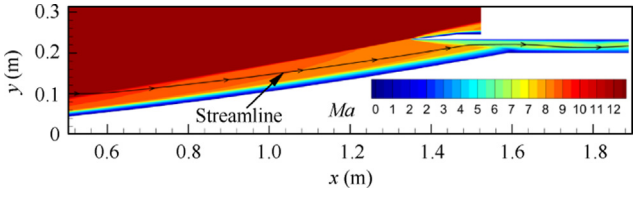

Fig. B1 Central streamline and Mach number contours inside thermochemical non-equilibrium flow field at Mach 12.

References

1. Smart MK. How much compression should a scramjet inlet do? *AIAA J* 2012;**50**(3):610–9.
2. Jiang ZL, Zhang ZJ, Liu YF, et al. Criteria for hypersonic airbreathing propulsion and its experimental verification. *Chin J Aeronaut* 2021;**34**(3):94–104.
3. Heiser W, Pratt D, Daley D, et al. *Hypersonic airbreathing propulsion*. Reston: AIAA; 1994.
4. Xu SC, Wang Y, Wang ZG, et al. Design and analysis of a hypersonic inlet with an integrated bump/forebody. *Chin J Aeronaut* 2019;**32**(10):2267–74.
5. Wang JF, Cai JS, Liu CZ, et al. Aerodynamic configuration integration design of hypersonic cruise aircraft with inward-turning inlets. *Chin J Aeronaut* 2017;**30**(4):1349–62.
6. Chen KS, Xu JL, Qin QH, et al. Three issues on nozzle thrust performance in cold-to-hot correlation considering variable specific heat effect. *Phys Fluids* 2022;**34**(7):076114.
7. Huang TL, Yue LJ, Ma SH, et al. Numerical investigation on flow nonuniformity-induced hysteresis in scramjet isolator. *Chin J Aeronaut* 2020;**33**(12):3176–88.
8. Yang QC, Bao W, Chetehouna K, et al. Thermal behavior of an isolator with mode transition inducing back-pressure of a dual-mode scramjet. *Chin J Aeronaut* 2017;**30**(2):595–601.
9. Hou LY, Weigand B, Banica M. Effects of staged injection on supersonic mixing and combustion. *Chin J Aeronaut* 2011;**24**(5):584–9.
10. Huang W, Du ZB, Yan L, et al. Supersonic mixing in airbreathing propulsion systems for hypersonic flights. *Prog Aerosp Sci* 2019;**109**:100545.
11. Sun MB, Wang HB, Zun C, et al. *Unsteady supersonic combustion*. Singapore: Springer Singapore; 2020.
12. Sun MB, Gong C, Zhang SP, et al. Spark ignition process in a scramjet combustor fueled by hydrogen and equipped with multi-cavities at Mach 4 flight condition. *Exp Therm Fluid Sci* 2012;**43**:90–6.
13. Marshall L, Bahm C, Corpening G, et al. Overview with results and lessons learned of the X-43A Mach 10 flight. Reston: AIAA; 2005. Report No.: AIAA-2005-3336.
14. Suraweera MV, Smart MK. Shock-tunnel experiments with a Mach 12 rectangular-to-elliptical shape-transition scramjet at offdesign conditions. *J Propuls Power* 2009;**25**(3):555–64.
15. Wise DJ, Smart MK. Experimental investigation of a three-dimensional scramjet engine at Mach 12. Reston: AIAA; 2015. Report No.: AIAA-2015-3650.
16. Toniato P, Gildfind DE, Andrianatos A, et al. Full free-stream Mach 12 scramjet testing in expansion tubes. Reston: AIAA; 2018. Report No.: AIAA-2018-3818.
17. Chan J, Sislian JP, Alexander D. Numerically simulated comparative performance of a scramjet and shcramjet at Mach 11. *J Propuls Power* 2010;**26**(5):1125–34.
18. Yao W, Liu H, Xue LJ, et al. Performance analysis of a strut-aided hypersonic scramjet by full-scale IDDES modeling. *Aerosp Sci Technol* 2021;**117**:106941.
19. Zhang ZJ, Ma KF, Zhang WS, et al. Numerical investigation of a Mach 9 oblique detonation engine with fuel pre-injection. *Aerosp Sci Technol* 2020;**105**:106054.
20. Zhang KY. *Hypersonic curved compression inlet and its inverse design*. Singapore: Springer Singapore; 2020.
21. Zhuang Y, Tan HJ, Wang WX, et al. Fractal features of turbulent/non-turbulent interface in a shock wave/turbulent boundary-layer interaction flow. *J Fluid Mech* 2019;**869**:R6.
22. Anderson JD. *Hypersonic and high-temperature gas dynamics*. 2nd ed. Reston: AIAA; 2006.
23. Dai CL, Sun B, Zhuo CF, et al. Numerical study of high temperature non-equilibrium effects of double-wedge in hypervelocity flow. *Aerosp Sci Technol* 2022;**124**:107526.
24. Dai CL, Sun B, Zhou SB, et al. Influence of high temperature non-equilibrium effects on Mach 12 scramjet inlet. *Acta Astronaut* 2022;**193**:237–54.
25. Xu SC, Wang Y, Wang ZG, et al. Unsteady behavior of hypersonic inlet unstart caused by high angle of attack. *Aerosp Sci Technol* 2022;**130**:107884.
26. Xiong B, Fan XQ, Wang Y. Parameterization and optimization design of a hypersonic inward turning inlet. *Acta Astronaut* 2019;**164**:130–41.
27. Minucci MAS, Nagamatsu HT. Experimental investigation of a 2-D scramjet inlet at Mach numbers of 8 to 18 and stagnation temperatures of 4100 K. Reston: AIAA; 1991. Report No.: AIAA-1991-0013.
28. Lai HT, Kim SC, Nagamatsu HT. Calculation of scramjet inlet with thick boundary-layer ingestion. *J Propuls Power* 1994;**10**(5):625–30.
29. Valentini P, Grover MS, Bisek N, et al. Molecular simulation of flows in thermochemical non-equilibrium around a cylinder using *ab initio* potential energy surfaces for N_2 + N and N_2 + N_2 interactions. *Phys Fluids* 2021;**33**(9):096108.
30. Hong QZ, Wang XY, Hu Y, et al. Development of a stagnation streamline model for thermochemical nonequilibrium flow. *Phys Fluids* 2020;**32**(4):046102.
31. Hao JA, Wen CY. Numerical investigation of oxygen thermochemical nonequilibrium on high-enthalpy double-cone flows. *Int J Heat Mass Transf* 2018;**127**:892–902.
32. Hao JA, Wen CY, Wang JY. Numerical investigation of hypervelocity shock-wave/boundary-layer interactions over a double-wedge configuration. *Int J Heat Mass Transf* 2019;**138**:277–92.
33. Vatansever D, Celik B. Unsteady shock interaction mechanisms of high enthalpy reacting flows over double wedges at Mach 7. *Phys Fluids* 2021;**33**(5):056110.
34. Fiévet R, Raman V. Effect of vibrational nonequilibrium on isolator shock structure. *J Propuls Power* 2018;**34**(5):1334–44.
35. Dai CL, Sun B, Zhou CS, et al. Numerical investigation of real-gas effect of inward-turning inlet at Mach 12. *Aerosp Sci Technol* 2021;**115**:106786.
36. Zuo FY, Mölder S, Hu SL. Thermochemical non-equilibrium effects on hypersonic wavecatcher intake at Mach 12. *Acta Astronaut* 2022;**198**:56–68.
37. Landau LD, Teller E. Theory of sound dispersion. *Physikalische Zeitschrift der Sowjetunion* 1936;**10**(1):34–43.
38. Millikan RC, White DR. Systematics of vibrational relaxation. *J Chem Phys* 1963;**39**(12):3209–13.
39. Park C. Assessment of two-temperature kinetic model for ionizing air. *J Thermophys Heat Transf* 1989;**3**(3):233–44.
40. McBride BJ, Zehe MJ, Gordon S. NASA Glenn coefficients for calculating thermodynamic properties of individual species. Washington, D.C.: NASA; 2002. Report No.: NASA/TP-2002-211556.
41. Gupta RN, Yos JM, Thompson RA, et al. A review of reaction rates and thermodynamic and transport properties for an 11-species air model for chemical and thermal nonequilibrium calculations to 30000 K. Washington, D.C.: NASA; 1990. Report No.: NASA-RP-1232.
42. Menter FR. Two-equation eddy-viscosity turbulence models for engineering applications. *AIAA J* 1994;**32**(8):1598–605.
43. Sarkar S. The pressure–dilatation correlation in compressible flows. *Phys Fluids A* 1992;**4**(12):2674–82.
44. White FM. *Viscous fluid flow*. New York: McGraw-Hill, Inc.; 1991.
45. Liang G, Huang HX, Tan HJ, et al. Shock train/glancing shock/boundary layer interaction in a curved isolator with sidewall contraction. *Phys Fluids* 2022;**34**(11):116106.
46. Zhang WL, Shi ZW, Zhang CH, et al. A study on flow control in a hypersonic inlet using a plasma synthetic jet actuator. *Phys Fluids* 2022;**34**(10):106109.
47. Wilke CR. A viscosity equation for gas mixtures. *J Chem Phys* 1950;**18**(4):517–9.

48. Gnoffo P. Point-implicit relaxation strategies for viscous, hypersonic flows. *Computational methods in hypersonic aerodynamics*, 1992, NASA; Washington, D.C, 115–51.
49. Batten P, Clarke N, Lambert C, et al. On the choice of wavespeeds for the HLLC Riemann solver. *SIAM J Sci Comput* 1997;**18**(6):1553–70.
50. Huang JK, Zhao X, Jiang H. Numerical simulation of the atomization of liquid transverse jet in supersonic airflow. *Phys Fluids* 2021;**33**(5):052114.
51. Muir HA, Nikiforakis N. Numerical modeling of imposed magnetohydrodynamic effects in hypersonic flows. *Phys Fluids* 2022;**34**(10):107114.
52. Harten A. High resolution schemes for hyperbolic conservation laws. *J Comput Phys* 1983;**49**(3):357–93.
53. Holden MS, Wadhams TP, MacLean MG, et al. Measurements of real gas effects on regions of laminar shock wave/boundary layer interaction in hypervelocity flows for "blind' code validation studies. Reston: AIAA; 2013. Report No.: AIAA-2013-2837.
54. Coleman GT, Stollery JL. Heat transfer from hypersonic turbulent flow at a wedge compression corner. *J Fluid Mech* 1972;**56**(4):741–52.
55. Jiang H, Liu J, Luo S, et al. Thermochemical non-equilibrium effects on hypersonic shock wave/turbulent boundary-layer interaction. *Acta Astronaut* 2022;**19**:1–14.
56. Tu GH, Deng XG, Mao ML. Assessment of two turbulence models and some compressibility corrections for hypersonic compression corners by high-order difference schemes. *Chin J Aeronaut* 2012;**25**(1):25–32.
57. Zhang XH, Wu YZ, Wang JF. Turbulence models for accurate aerothermal prediction in hypersonic flows. *Mod Phys Lett B* 2010;**24**(13):1345–8.
58. Passiatore D, Sciacovelli L, Cinnella P, et al. Thermochemical non-equilibrium effects in turbulent hypersonic boundary layers. *J Fluid Mech* 2022;**941**:A21.
59. Tahir R, Molder S, Timofeev E. Unsteady starting of high Mach number air inlets —A CFD study. Reston: AIAA; 2003. Report No.: AIAA-2003-5191.
60. Wu J, Yu AY, He YY, et al. Self-starting simulation of a hypersonic inlet with variable free stream condition. *J Appl Fluid Mech* 2020;**13**(6):1683–91.
61. Donde P, Marathe A, Sudhakar K. Starting in hypersonic intakes. Reston: AIAA; 2006. Report No.: AIAA-2006-4510.
62. A Yu, D Yang, J Wu, et al., The numerical simulation techniques research and preliminary experimental validation of the start characteristics for a two-dimensional hypersonic inlet. *Progress in propulsion physics* – 11, 2019, Les Ulis: EDP Sciences, 729–46.
63. Bernardini M, Asproulias I, Larsson J, et al. Heat transfer and wall temperature effects in shock wave turbulent boundary layer interactions. *Phys Rev Fluids* 2016;**1**(8):084403.